JEM Journal of Experimental Medicine

ARTICLE

Fetal MAVS and type I IFN signaling pathways control ZIKV infection in the placenta and maternal decidua

Yael Alippe[1], Leran Wang[2], Reyan Coskun[1,3], Stéfanie P. Muraro[4], Fang R. Zhao[1], Michelle Elam-Noll[1], J. Michael White[5], Daiana M. Vota[6], Vanesa C. Hauk[6], Jeffrey I. Gordon[2,3,5], Scott A. Handley[2], and Michael S. Diamond[1,2,7,8,9]

The contribution of placental immune responses to congenital Zika virus (ZIKV) syndrome remains poorly understood. Here, we leveraged a mouse model of ZIKV infection to identify mechanisms of innate immune restriction exclusively in the fetal compartment of the placenta. ZIKV principally infected mononuclear trophoblasts in the junctional zone, which was limited by mitochondrial antiviral-signaling protein (MAVS) and type I interferon (IFN) signaling mechanisms. Single nuclear RNA sequencing revealed MAVS-dependent expression of IFN-stimulated genes (ISGs) in spongiotrophoblasts but not in other placental cells that use alternate pathways to induce ISGs. ZIKV infection of *Ifnar1*$^{-/-}$ or *Mavs*$^{-/-}$ placentas was associated with greater infection of the adjacent immunocompetent decidua, and heterozygous *Mavs*$^{+/-}$ or *Ifnar1*$^{+/-}$ dams carrying immunodeficient fetuses sustained greater maternal viremia and tissue infection than dams carrying wild-type fetuses. Thus, MAVS-IFN signaling in the fetus restricts ZIKV infection in junctional zone trophoblasts, which modulates dissemination and outcome for both the fetus and the pregnant mother.

Introduction

Zika virus (ZIKV) is a mosquito-borne flavivirus that can be transmitted vertically, resulting in adverse pregnancy outcomes including fetal growth restriction, microcephaly, fetal demise, and developmental disorders observed at or after birth (Brasil et al., 2016; Sarno et al., 2016; Ventura et al., 2016). Vertical transmission of ZIKV usually occurs via spread from the maternal circulation to the maternal decidua and then to the fetal-derived placenta, where it infects several cell types including trophoblasts and endothelial cells (Cao et al., 2017; Coyne and Lazear, 2016). However, the basis for cell tropism in the placenta is not well understood.

ZIKV-induced fetal pathology depends on the gestational age at the time of infection (Brasil et al., 2016; Kleber de Oliveira et al., 2016), as the stage in pregnancy influences maternal immunity, maternal–fetal barrier integrity, and ZIKV tropism (Ander et al., 2019). Studies with human primary placental cultures have shown that the decidua and mononuclear trophoblasts are more susceptible to ZIKV infection at early gestational stages (Sheridan et al., 2017). At later stages, the placenta becomes more resistant to ZIKV infection, possibly due to type III interferon (IFN-λ) signaling in syncytiotrophoblasts (SynT) (Bayer et al., 2015; Delorme-Axford et al., 2013). Nonetheless, adverse fetal outcomes occur even when congenital ZIKV infection happens at later stages of pregnancy (Brasil et al., 2016), and may be associated with disruption of the trophoblast layer due to proinflammatory type I IFN-α/β responses (Yockey et al., 2018). Apart from this, systemic maternal immune responses may affect, or be affected by, ZIKV infection in placental and fetal tissues. Indeed, prolonged maternal viremia is associated with worsened fetal outcomes (Pomar et al., 2021; Suy et al., 2016).

Due to limitations in obtaining human fetal samples, vertical transmission and congenital ZIKV have been studied in animal models, including mice and non-human primates

---

[1]Department of Medicine, Washington University School of Medicine, St. Louis, MO, USA; [2]Department of Pathology and Immunology and Center for Genome Sciences, Lab and Genomic Medicine, Washington University School of Medicine, St. Louis, MO, USA; [3]The Edison Family Center for Genome Sciences and Systems Biology, Washington University School of Medicine, St. Louis, MO, USA; [4]Campinas State University, Laboratory of Emerging Viruses, Campinas, Brazil; [5]Center for Gut Microbiome and Nutrition Research, Washington University School of Medicine, St. Louis, MO, USA; [6]Universidad de Buenos Aires—CONICET, Instituto de Química Biológica de la Facultad de Ciencias Exactas y Naturales, Buenos Aires, Argentina; [7]Department of Molecular Microbiology, Washington University School of Medicine, St. Louis, MO, USA; [8]Andrew M. and Jane M. Bursky the Center for Human Immunology and Immunotherapy Programs, Washington University School of Medicine, St. Louis, MO, USA; [9]Center for Vaccines and Immunity to Microbial Pathogens, Washington University School of Medicine, St. Louis, MO, USA.

M. Elam-Noll died on February 25, 2023. Correspondence to Michael S. Diamond: mdiamond@wustl.edu.

Rockefeller University Press
J. Exp. Med. 2024 Vol. 221 No. 9 e20240694
https://doi.org/10.1084/jem.20240694

(Morrison and Diamond, 2017). Because ZIKV antagonizes human but not mouse STAT2 (Gorman et al., 2018; Grant et al., 2016; Kumar et al., 2016), immunocompetent mice are relatively resistant to ZIKV infection, especially when the virus is administered by subcutaneous injection (Lazear et al., 2016). Thus, in many mouse models, ZIKV pathogenesis during pregnancy has been investigated in dams deficient in type I IFN signaling. Despite anatomical and functional differences between human and mouse placentas, mouse models recapitulate features of human infection, including vertical transmission, fetal growth restriction, and fetal demise (Jagger et al., 2017; Miner et al., 2016; Yockey et al., 2018). In some of these studies, type I IFN signaling in the fetus restricts ZIKV infection but nonetheless is associated with greater fetal death (Yockey et al., 2018). Other reports describe how type III IFN signaling in the maternal decidua controls ZIKV infection and prevents severe fetal outcomes when infection occurs at late but not early stages of pregnancy (Casazza et al., 2022; Jagger et al., 2017). A limitation of these models for understanding innate immunity at the maternal–fetal interface is the confounding effects of enhanced infection of the immunocompromised dam lacking type I IFN signaling. As an alternative approach, ZIKV has been administered by intravenous or intrauterine injection in immunocompetent dams, which bypasses the inhibitory type I IFN responses in peripheral tissues that limit spread to the decidua. In these models, ZIKV infection caused placental infection and damage, fetal growth restriction, and fetal demise, albeit to varying degrees (Cugola et al., 2016; Szaba et al., 2018; Vermillion et al., 2017). Thus, the immunocompetent mouse placenta may be susceptible to ZIKV infection if the virus can access the maternal decidua, although the mechanisms underlying cell tropism and innate immune responses at this interface are undetermined.

Here, we used breeding schemes designed to identify effects of specific innate immune signaling pathways in the fetal compartment of the placenta in the context of intact maternal immune responses. Intravenous inoculation of ZIKV in immunocompetent dams at mid-gestation resulted in infection of the maternal decidua and the junctional zone of immunocompetent placentas and growth restriction of the developing fetus. A loss of fetal mitochondrial antiviral-signaling protein (MAVS) signaling, which is downstream of RIG-I–like viral sensors, or type I IFN signaling (through loss of IFNAR1 engagement or downstream STAT1 signaling), promoted ZIKV infection throughout the junctional zone and its spread to the fetus. Single nuclear RNA sequencing (snRNAseq) analysis of ZIKV-infected wild-type (WT) or *Mavs*$^{-/-}$ placentas revealed MAVS-dependent, cell-intrinsic induction of IFN-stimulated (ISG) and viral-stimulated (VSG) genes in permissive junctional zone cells (spongiotrophoblasts [SpT]) and suggested the existence of MAVS-independent host defense pathways in other cells of the fetal placenta. Notably, enhanced ZIKV infection in SpT due to a lack of fetal MAVS and IFN signaling was sufficient to cause greater infection in adjacent immunocompetent fetoplacental and decidual units as well as in the dam, suggesting that ZIKV replication in the placenta can modulate infection kinetics and possibly outcomes in the immunocompetent pregnant host.

Results

Placental ZIKV infection in immunocompetent mice

Because ZIKV fails to evade type I IFN responses in mice (Grant et al., 2016; Kumar et al., 2016), infection of immunocompetent pregnant dams is aborted after subcutaneous inoculation and does not cause infection of the placenta or developing fetus (Miner et al., 2016). To overcome this limitation, one approach has been to use human *STAT2* knock-in/murine *Stat2* knockout (KO) mice to surmount the species-dependent innate immune restriction of ZIKV (Gorman et al., 2018; Grant et al., 2016; Kumar et al., 2016). Alternatively, others have inoculated pregnant immunocompetent mice by intravenous injection, which bypasses peripheral antiviral immune responses, and results in vertical transmission of ZIKV (Cugola et al., 2016; Szaba et al., 2018). To study placental immune responses to ZIKV, whereby some of the fetal placental units are immunodeficient but the dam is immunocompetent, we leveraged breeding schemes (+/− female × −/− male) and the intravenous inoculation model in WT C57BL/6 mice using a mouse-adapted ZIKV strain (Dakar 41525 NS4B-G18R, hereafter ZIKV) (Gorman et al., 2018).

To first establish the vertical transmission model, we inoculated WT dams that had been mated to WT sires with ZIKV (Dakar 41525 strain) at mid-gestational age (embryonic day 9.5; E9.5) after placentation is established and most trophoblast subtypes are present (Elmore et al., 2022; Hemberger et al., 2020; Isaac et al., 2014). Intravenous inoculation with 3.5×10^5 or 3.5×10^6 focus-forming units (FFU) of ZIKV induced greater fetal demise at E17.5 than mock-infected dams or those infected with a lower dose (3.5×10^4 FFU) of ZIKV (Fig. 1 A). Mild, but statistically significant, fetal growth restriction was seen with the 3.5×10^6 FFU dose but not with the lower doses ($n = 4$–8 dams per group; $P < 0.0001$, Fig. 1 B). These outcomes were associated with detectable viral RNA in the maternal spleen, maternal decidua, and the fetal compartment of the placenta. However, we detected little, if any, ZIKV RNA in the fetal heads (Fig. 1 C), as previously reported for immunocompetent mice inoculated with similar doses (Szaba et al., 2018).

Viral RNA in situ hybridization (ISH) studies in tissues harvested at E17.5 (corresponding to 8 days post-infection [dpi]) showed that ZIKV preferentially infects the junctional zone of the fetal placenta and proximal decidua (Fig. 1 D). In the junctional zone, we detected ZIKV RNA in *Prl7a2*$^+$ SpT and *Pcdh12*$^+$ glycogen cells (GlyC) (Marsh and Blelloch, 2020; Simmons et al., 2008; Zhou et al., 2021) (Fig. 2 A, top panel). We observed a similar pattern of infection using *Prl3b1*, another SpT marker (Marsh and Blelloch, 2020; Simmons et al., 2008; Zhou et al., 2021) (Fig. 2 A, bottom panel, and Fig. 2 B, inset 1). We generally did not observe ZIKV staining in the labyrinth zone, except in some *Prl3b1*$^+$ SpTs present in this layer (Fig. 2 A, stars), which are distinguished from sinusoidal trophoblast giant cells (S-TGC) by differential expression of *Ctsq* (Simmons et al., 2007) (Fig. 2 A, bottom panel). ZIKV RNA also was found in parietal trophoblast giant cells (P-TGC) underlying the decidua, which express *Prl3b1*

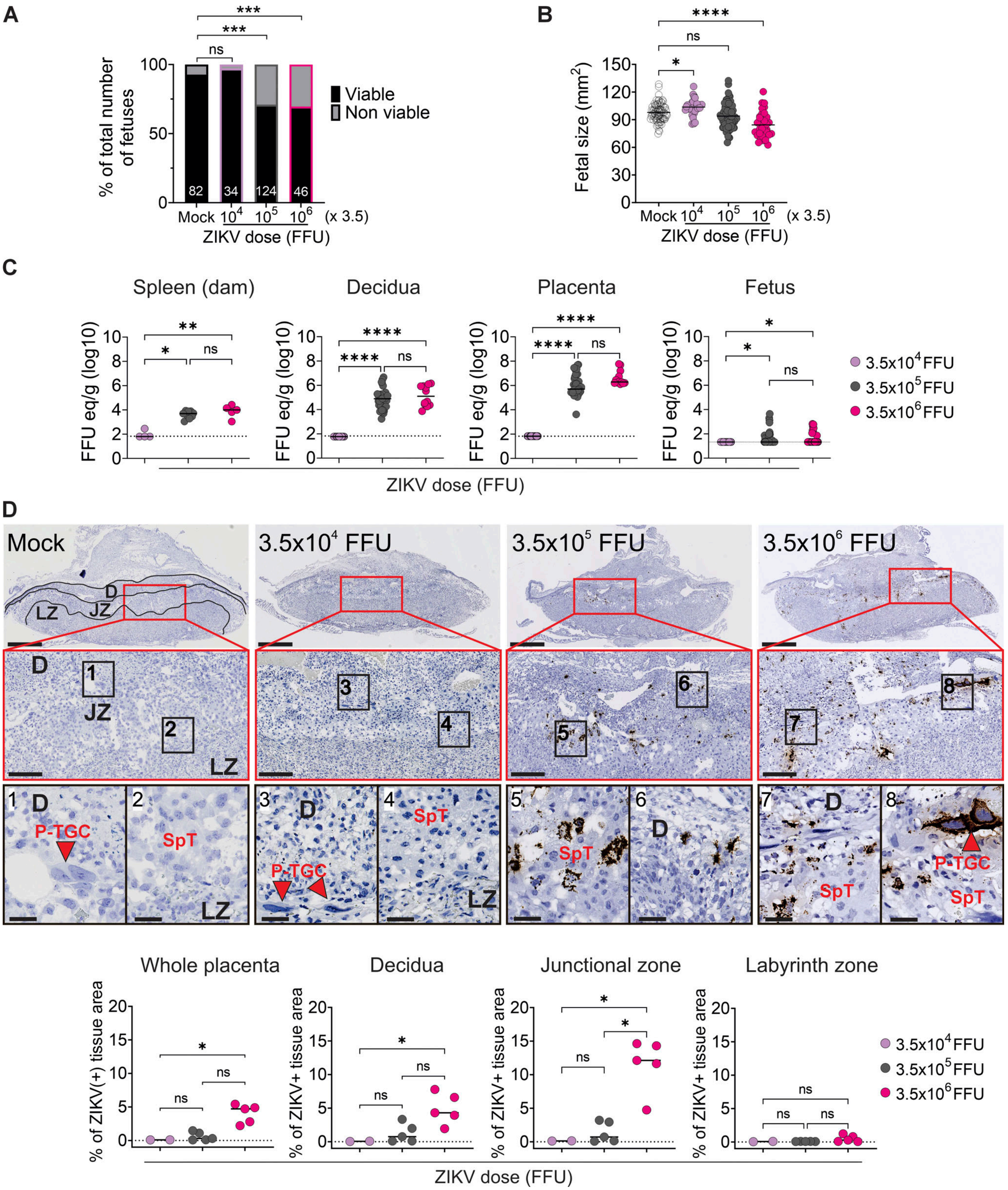

Figure 1. **ZIKV induces fetal growth restriction and infection of the junctional zone in immunocompetent mice. (A and B)** WT C57BL/6 dams were inoculated via intravenous injection at E9.5 with saline or increasing doses of ZIKV (3.5 × 10^4, 3.5 × 10^5, or 3.5 × 10^6 FFU), and outcomes were assessed at E17.5 (8 dpi). **(A)** Fetal viability: percentage of resorbed or unviable fetuses/total fetuses (7% in naive, 3% for 3.5 × 10^4 FFU dose, and 30% for 3.5 × 10^5 and 3.5 × 10^6 FFU doses). **(B)** Fetal size was determined as crown-rump length × occipital-frontal diameter. **(A and B)** Data are from three experiments; *n* (dams) = 8, 4, 9, and 5 per group (mock, 3.5 × 10^4, 3.5 × 10^5, or 3.5 × 10^6 FFU, respectively); the number of fetuses is denoted above columns in A; data points in B indicate individual fetuses. **(C)** ZIKV RNA levels in maternal spleen, decidua, placenta, and fetus. Data are from three experiments: *n* (dams) = 4, 9 and 5, and *n* (fetuses and placentas) = 29, 37, and 12 per dose (3.5 × 10^4, 3.5 × 10^5, or 3.5 × 10^6 FFU, respectively). **(D)** Top: ISH of ZIKV RNA in placentas from dams inoculated with 3.5 × 10^4, 3.5 × 10^5, or 3.5 × 10^6 FFU. Placenta images at 2.5× magnification (scale bars: 1 mm); red insets at 10× magnification (scale bars: 250 µm), and black

insets at 40× magnification (scale bars: 50 µm). Red arrowheads, P-TGC; numbers indicate the corresponding inset. D, decidua; JZ, junctional zone; LZ, labyrinth zone. Bottom: quantification of ZIKV-positive areas was performed by semiautomated analysis using QuPath software (Bankhead et al., 2017). Each data point represents the average of at least two tissue sections from the same placenta. *n* = 2 (3.5×10^4 FFU) and *n* = 5 (3.5×10^5 and 3.5×10^6 FFU) placentas from two dams per group, three independent experiments. Statistical analysis: (A) Chi-squared test with Bonferroni correction (each dose compared to mock; $^{***}P_{adj} < 0.001$, ns, not significant); (B and D) One-way ANOVA with Dunnett's post-test; ($^{*}P < 0.05$, $^{****}P < 0.0001$, ns, not significant); (C) Kruskal–Wallis ANOVA with Dunn's post-test ($^{*}P < 0.05$, $^{**}P < 0.01$, $^{****}P < 0.0001$, ns, not significant). Dotted lines represent the limit of detection (LOD).

---

but not *Ctsq*, and feature prominently large nuclei (Elmore et al., 2022; Simmons et al., 2007) (Fig. 1 D, red arrowheads, and Fig. 2 B, inset 2). Finally, ZIKV staining was detected in the decidua in both invasive GlyC and vimentin^{+} decidual stromal cells (Fig. 2 C).

At the 3.5×10^5 or 3.5×10^6 FFU doses, ZIKV infection resulted in a decrease in the total placental area, which reflects reductions in the decidua and junctional zone, but not the labyrinth zone (Fig. S1 A). Histological analysis showed that placentas from ZIKV-infected dams displayed cellular and structural changes in all layers compared with mock-infected dams. In the decidua, we observed varying degrees of leukocyte infiltration depending on the ZIKV dose (Fig. S1 B). Foci of cell necrosis in the junctional zone, which also can be physiological at this gestational stage (Detmar et al., 2019), were observed at the higher but not the lower ZIKV dose, and this was associated with reductions in staining for the pan-trophoblast marker cytokeratin 7 (CK7), loss of nuclei, and vascular congestion in the SpT cell layer (Fig. S1, B and C). The higher inoculating dose of ZIKV also resulted in an alteration of the mesenchyme-vascular architecture in the labyrinth zone, as reflected by changes in vimentin staining (Fig. S1 D). Thus, in this immunocompetent mouse model, infection of the dam with ZIKV Dakar 41525 induced changes in placental structure and function that impacted fetal development, as reported for other ZIKV strains (Cugola et al., 2016; Szaba et al., 2018).

We next performed a time course to study the kinetics of viral infection at the maternal–fetal interface. After inoculating pregnant dams at E9.5 with 3.5×10^6 FFU of ZIKV, levels of viral RNA in the maternal decidua peaked at 4 dpi (E13.5) and remained elevated through 8 dpi (E17.5). However, levels in the fetal placenta increased over time, with approximately fivefold higher levels ($P < 0.001$) measured at E17.5 (8 dpi) than at E11.5 (2 dpi) (*n* = 2–3 dams and 6–7 placentas/time point). Low levels of viral RNA were present in the fetal heads, with a small peak at E13.5 (4 dpi) (Fig. 2 D). We also observed a small, but statistically significant, increase in yield of infectious virus over time in the fetal placenta but not in the maternal decidua (Fig. 2 E). These data suggest that the fetal compartment acts as a replicative niche for ZIKV, although susceptible cells in the decidua also might act as reservoirs as previously proposed (Guzeloglu-Kayisli et al., 2020). Increased viral infection in the fetal placenta correlated with higher levels of proinflammatory chemokine and cytokines (e.g., CCL5, CXCL10, CCL2, CXCL1, IL-2, G-CSF) in this compartment, especially at later time points (Fig. S1 E). Overall, our data suggest that intravenous injection of ZIKV in immunocompetent dams results in infection of the decidua and placenta, which leads to inflammation at the maternal–fetal interface, placental damage, fetal growth restriction, and, in some instances, fetal demise.

A MAVS–IFNAR1 signaling pathway restricts ZIKV infection in the placenta

One pathway for induction of type I IFNs after flavivirus infection is through recognition of viral RNA by RIG-I–like receptors (RLRs), such as RIG-I and MDA5, and downstream MAVS signaling (Loo and Gale, 2011). We hypothesized that the MAVS and IFNAR1 signaling pathways in the fetal compartment might have a role in restricting transmission of ZIKV across the maternal–fetal interface. To study these pathways exclusively in the fetal placenta, we crossed *Mavs*$^{+/-}$ or *Ifnar1*$^{+/-}$ heterozygous dams with the corresponding heterozygous or KO sires to obtain immunodeficient fetal placentas (*Mavs*$^{-/-}$ or *Ifnar1*$^{-/-}$) carried by dams with one functional *Mavs* or *Ifnar1* allele (see Materials and methods). We inoculated these dams intravenously with 3.5×10^5 FFU of ZIKV at E9.5 and euthanized them at E17.5 for tissue collection.

In *Mavs*$^{+/-}$ females mated with either *Mavs*$^{+/-}$ or *Mavs*$^{-/-}$ males, infection of the deciduas adjacent to *Mavs*$^{-/-}$ placentas was ~10-fold higher ($P < 0.0001$) than in decidua from WT × WT crosses (Fig. 3 A, left). Infection levels were similarly increased in *Ifnar1*$^{+/-}$ deciduas adjacent to *Ifnar1*$^{-/-}$ placentas, which were obtained by crossing *Ifnar1*$^{+/-}$ females with either *Ifnar1*$^{+/-}$ or *Ifnar1*$^{-/-}$ males (Fig. 3 B, left). Haploinsufficiency was not observed as ZIKV infection was equivalent in the maternal deciduas or placentas of WT, *Mavs*$^{+/-}$, or *Ifnar1*$^{+/-}$ dams after crossing to WT sires (Fig. 3, A and B, right). Thus, the higher levels of virus in the *Mavs*$^{+/-}$ or *Ifnar1*$^{+/-}$ decidua adjacent to immunodeficient placentas suggest that virus may spread from the highly infected adjacent tissues; indeed, *Mavs*$^{-/-}$ or *Ifnar1*$^{-/-}$ placentas had ~30-fold higher levels ($P < 0.0001$) of ZIKV RNA than those from WT dam and sire matings (*n* = 5 dams/group; Fig. 3, C and D, left).

Mavs$^{-/-}$ fetuses derived from *Mavs*$^{+/-}$ × *Mavs*$^{-/-}$ or *Mavs*$^{+/-}$ matings also had higher ZIKV RNA levels than those from WT × WT crosses (Fig. 4 A, left). Infection trended higher in *Ifnar1*$^{-/-}$ fetuses derived from *Ifnar1*$^{+/-}$ × *Ifnar1*$^{+/-}$ or *Ifnar1*$^{-/-}$ crosses (Fig. 4 B, left). Haploinsufficiency effects were ruled out as ZIKV RNA was undetectable in fetuses from WT × WT, *Mavs*$^{+/-}$ × WT, or *Ifnar1*$^{+/-}$ × WT crosses (Fig. 4, A and B, right). These results suggest that deficiencies in MAVS and type I IFN signaling in the fetal placenta cause greater infection at the fetal–maternal interface, which can spread to neighboring fetoplacental units. To confirm the effects of deficiencies of IFN signaling, we evaluated ZIKV infection in placentas and fetuses deficient in STAT1, which acts downstream of type I IFN receptor engagement. When *Stat1*$^{+/-}$ dams mated to *Stat1*$^{-/-}$ sires were inoculated at

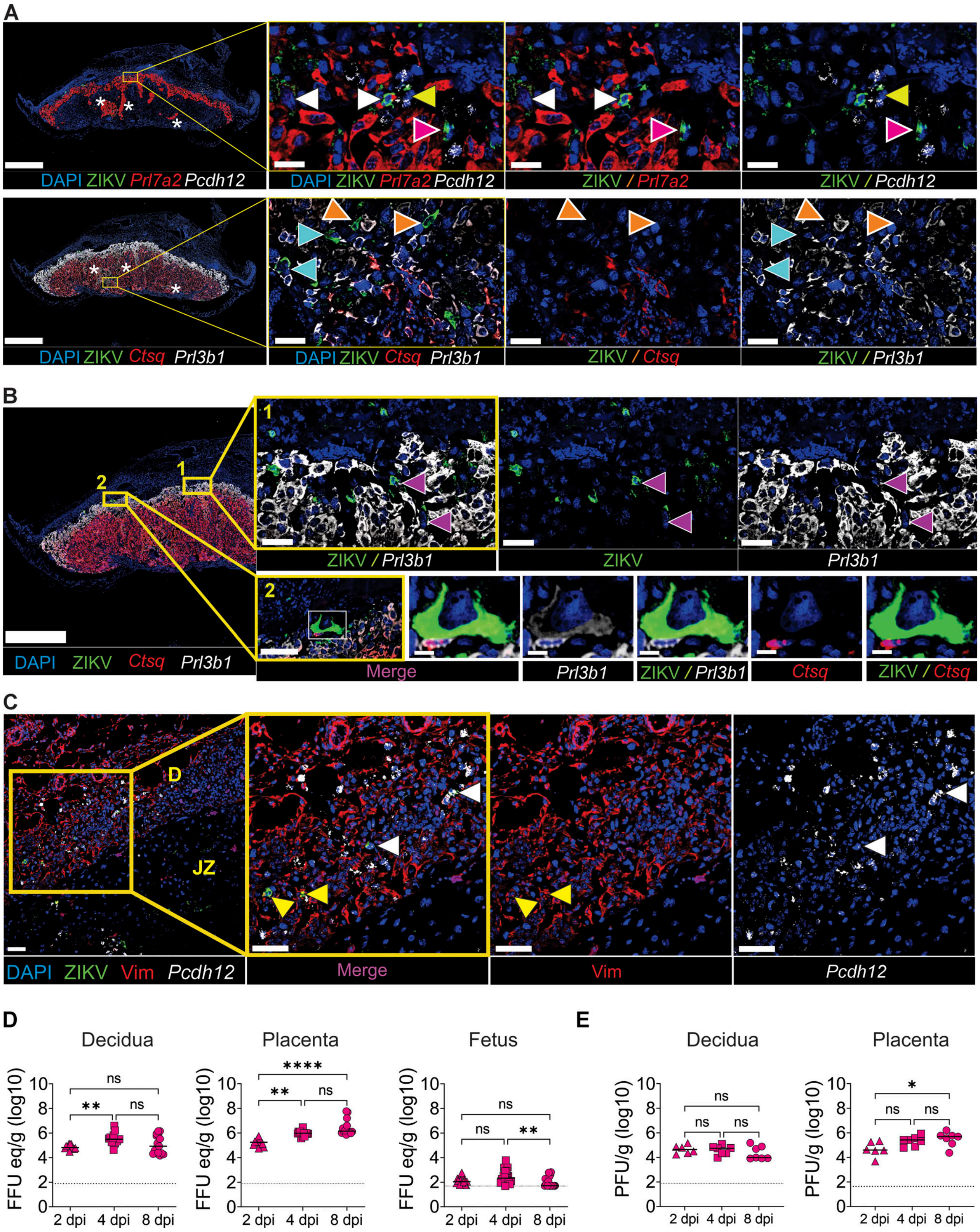

Figure 2. **ZIKV targets specific cell types in the decidua and junctional zones. (A–C)** Representative images of multiplexed FISH of WT placentas after infection with 3.5 × 10^6 FFU ZIKV at 8 dpi. **(A)** ZIKV, *Prl7a2* (SpT), *Pcdh12* (GlyC) RNA (top panel), and ZIKV, *Prl3b1* (SpT, S-TGC, and P-TGC), and *Ctsq* (S-TGC) (bottom panel). Placenta images at 2.5× magnification (scale bars: 1 mm); yellow insets: maximum projection of three to four confocal z-stacks taken at 20× magnification (scale bars: 50 µm). White arrowheads, SpT; yellow arrowheads, GlyC; magenta arrowheads, ZIKV staining only; asterisks and orange arrowheads, SpT in labyrinth zone; light blue arrowheads, S-TGC. **(B)** ZIKV, *Prl3b1* (SpT, S-TGC, and P-TGC), and *Ctsq* (S-TGC). Placenta images at 2.5× magnification (scale bars: 1 mm); numbers indicate the corresponding inset. Yellow inset 1: maximum projection of three to four confocal z-stacks taken at 20× magnification

(scale bars: 50 µm; purple arrowheads, SpT); yellow inset 2: scale bars = 100 µm; white insets zoomed at 200% (scale bars = 20 µm). **(C)** *ZIKV*, *Pchd12* (GlyC), and vimentin (endothelial and stromal cells). Maximum projection of three to four confocal Z-stacks taken at 20× magnification of the decidua (D) and junctional zone (JZ), and insets zoomed 200% (scale bars: 50 µm; white arrowheads, GlyC; yellow arrowheads, decidual stromal cells). **(A–C)** Samples are from two experiments, $n = 2$ dams, 2 placentas each. **(D and E)** Time course analysis of ZIKV infection by qRT-PCR (viral RNA) (D) or plaque assay (infectious virus) (E) in the decidua and the fetal placenta at 2 dpi (E11.5), 4 dpi (E13.5), and 8 dpi (E17.5) after inoculation with 3.5×10^6 FFU ZIKV. Each data point represents an individual decidua or fetal placenta from $n = 2$ (2 and 4 dpi) and $n = 3$ (8 dpi) dams from two experiments. Statistical analysis: (D and E) Kruskal–Wallis ANOVA with Dunn's post-test (*$P < 0.05$, **$P < 0.01$, ****$P < 0.0001$, ns, not significant). The dotted lines represent the LOD.

E9.5, we observed higher ZIKV burden at E17.5 in *Stat1*$^{-/-}$ placentas and fetuses compared with those obtained from separate WT × WT crosses (Fig. 4 C). Higher levels of ZIKV RNA also were detected in *Stat1*$^{+/-}$ fetuses derived from *Stat1*$^{+/-}$ × *Stat1*$^{-/-}$ crosses. Taken together, these results suggest a key role for innate immune sensing and signaling via MAVS, type I IFN, and STAT1 in the fetal compartment of the placenta.

We next evaluated whether other pathogen recognition receptor and antiviral signaling pathways impacted ZIKV infection at the maternal–fetal interface; we focused on key sensing and downstream signaling pathways that had not been assessed previously in pregnancy models. Toll-like receptors (TLRs) such as TLR7/8 or TLR9 can recognize flavivirus RNA in endosomes and activate type I IFN signaling through the MyD88 adaptor protein (Lester and Li, 2014; Suthar et al., 2013). However, an absence of fetal TLR7 or TLR9 expression did not result in a significantly increased viral burden in the decidua, placenta, or fetus (Fig. S2, A and B). Unexpectedly, and for reasons that remain unclear, a loss of fetal expression of MyD88, which acts downstream of several TLRs as well as IL1R, paradoxically resulted in lower viral burden in the decidua and placenta (Fig. S2 C). We also observed no impact in the decidua, placenta, or fetus due to a lack of STING, a signaling adaptor of the cGAS pathway that restricts ZIKV infection in vitro in fibroblasts and glioma cells and in vivo in the developing *Drosophila* brain (Ding et al., 2018; Li et al., 2022; Liu et al., 2018) (Fig. S2 D). Finally, we tested the effects of type III IFN-λ signaling in our model by crossing *Ifnlr1*$^{+/-}$ dams with *Ifnlr1*$^{-/-}$ sires. Levels of ZIKV RNA in the deciduas, placentas, and fetuses from *Ifnlr1*$^{+/-}$ × *Ifnlr1*$^{-/-}$ crosses were equivalent to those from WT × WT crosses (Fig. S2 E), which agrees with a study showing a dominant antiviral role of IFN-λ in the maternal decidua, but not in the fetal placenta (Casazza et al., 2022). Overall, these data suggest that fetal TLR7, TLR9, MyD88, STING, and IFN-λ do not have substantive antiviral effects on ZIKV burden in the fetal placenta and developing fetus.

MAVS and type I IFN signaling restrict ZIKV infection in the junctional zone of the placenta

We performed viral RNA ISH to address how MAVS and IFNAR1 deficiencies affect ZIKV tropism in the placenta and adjacent decidua. Deciduas associated with *Mavs*$^{+/-}$ or *Ifnar1*$^{+/-}$ placentas showed relatively similar levels and distributions of ZIKV RNA (Fig. 5 A and see Fig. 1 D) compared with those adjacent to WT placentas obtained from WT × WT matings. In contrast, *Mavs*$^{-/-}$ and *Ifnar1*$^{-/-}$ placentas showed intense staining of viral RNA in the junctional zone and greater amounts in the adjacent *Mavs*$^{+/-}$ or *Ifnar1*$^{+/-}$ maternal decidua but not in the labyrinth zone (Fig. 5 A). Within the junctional zone, we observed concentrated ZIKV RNA staining in the SpT layer of *Mavs*$^{-/-}$ placentas, with preferentially increased signal in P-TGCs in *Ifnar1*$^{-/-}$ placentas (Fig. 5 A). Multiplexed fluorescence-based ISH (FISH) and FISH combined with immunofluorescence analysis confirmed the increased susceptibility of SpTs (*Prl7a2*$^{+}$) to ZIKV infection in *Mavs*$^{-/-}$ and *Ifnar1*$^{-/-}$ placentas (Fig. 5 B) compared with WT placentas (see Fig. 2, A and B). We also detected higher amounts of ZIKV RNA in P-TGCs (*Ctsq*$^{-}$, *Prl3b1*$^{+}$; oversized nuclei) in *Ifnar1*$^{-/-}$ compared with *Mavs*$^{-/-}$ placentas (Fig. 5 C). We observed little ZIKV RNA staining in S-TGCs (*Ctsq*$^{+}$/*Prl3b1*$^{+}$) underlying the junctional zone in placentas of both genotypes (Fig. 5 C). ZIKV RNA also was sporadically detected in GlyCs (*Phcd12*$^{+}$) in the junctional zone of *Mavs*$^{-/-}$ or *Ifnar1*$^{-/-}$ placentas (Fig. 5 B), including ones invading the decidua, and in vimentin^{+} maternal stromal cells (Fig. S3 A). For most fetuses, we did not detect viral RNA by ISH, regardless of the genotype (Fig. S3 B). Nonetheless, in some ZIKV-infected *Ifnar1*$^{-/-}$ fetuses, ZIKV RNA staining was apparent and associated with abundant infection in the labyrinth zone of the placenta (two of six *Ifnar1*$^{-/-}$ fetuses; Fig. S3 C). In these placental samples, ZIKV RNA localized to the fetoplacental endothelium (Vim^{+}/*CD31* [*Pecam1*]$^{+}$) (Fig. S3 E) and syncytial cells (CK7^{+}/*Ctsq*$^{-}$), but not S-TGC (CK7^{+}/*Ctsq*$^{+}$) (Fig. S3 F). Thus, these results suggest potential actions of type I IFN signaling beyond the junctional zone of the placenta.

Persistent ZIKV viremia occurs in pregnant, but not non-pregnant, women (Driggers et al., 2016; Pomar et al., 2021). Because we observed increased ZIKV infection in the decidua of heterozygous dams carrying homozygous *Mavs*$^{-/-}$ or *Ifnar1*$^{-/-}$ fetuses, we hypothesized that higher infection in the fetal placenta might spread back to the dam and result in increased maternal infection. To evaluate this hypothesis, we compared ZIKV infection in non-pregnant and pregnant WT, *Mavs*$^{+/-}$, or *Ifnar1*$^{+/-}$ females, with dams, respectively, bearing WT, *Mavs*$^{-/-}$, or *Ifnar1*$^{-/-}$ fetuses (Fig. 6). At 8 dpi, ZIKV RNA levels in the spleen of non-pregnant WT, *Mavs*$^{+/-}$, or *Ifnar1*$^{+/-}$ females were similar, and viral RNA was absent from the serum, uterus, or ovaries. Pregnant dams tended to have higher ZIKV RNA levels in the spleen and uterus than non-pregnant females. Viral burden in *Mavs*$^{+/-}$ and *Ifnar1*$^{+/-}$ dams mated with WT sires was comparable with WT dams mated with WT sires, whereas *Mavs*$^{+/-}$ and *Ifnar1*$^{+/-}$ dams carrying *Mavs*$^{-/-}$ or *Ifnar1*$^{-/-}$ fetuses had the highest levels of infection, including sustained viremia (Fig. 6). Despite these results, we did not observe weight loss or signs of clinical disease in any of the dams, consistent with previous results from ZIKV-infected immunocompetent mice (Lazear et al., 2016). These data suggest that pregnant dams do not clear ZIKV infection efficiently when MAVS or IFNAR1 signaling is deficient in the fetal compartment.

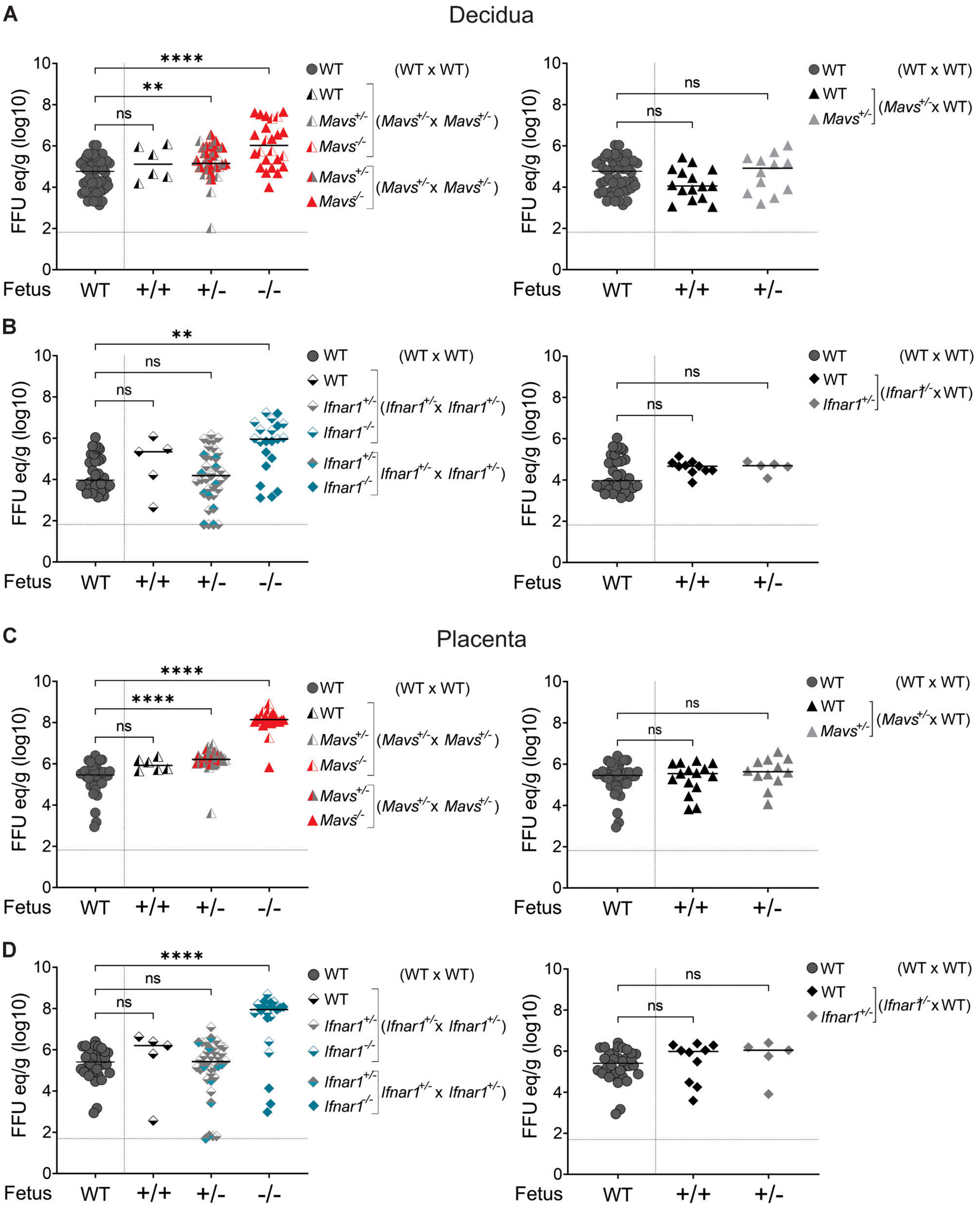

Figure 3. **MAVS and type I IFN signaling restrict ZIKV infection in the decidua and placenta. (A–D)** WT, *Mavs*$^{+/-}$, and *Ifnar1*$^{+/-}$ females were mated with WT, *Mavs*$^{+/-}$, *Mavs*$^{-/-}$, *Ifnar1*$^{+/-}$, or *Ifnar1*$^{-/-}$ males as indicated. Dams were inoculated by intravenous injection at E9.5 with 3.5 × 10^5 FFU of ZIKV, and viral burden was assessed at 8 dpi. For simplification, samples were grouped by fetal genotype, independent of the breeding scheme for the target genes. ZIKV RNA from maternal decidua (A and B) and fetal placenta (C and D). Fetal genotypes are indicated on the x-axis. Left: samples from the different crosses were grouped and identified with differently colored symbols, as indicated in the figure. Right: haploinsufficiency controls were performed by crossing heterozygous females with WT males, as denoted. Samples from maternal decidua were grouped by the genotype of the corresponding fetus. Data are from at least three experiments, with samples pooled from *n* = 5 dams per group. Statistical analysis: Kruskal–Wallis ANOVA with Dunn's post-test (comparison to samples from WT × WT matings; $^{**}P < 0.01$, $^{****}P < 0.0001$, ns, not significant). Dotted horizontal lines represent the LOD.

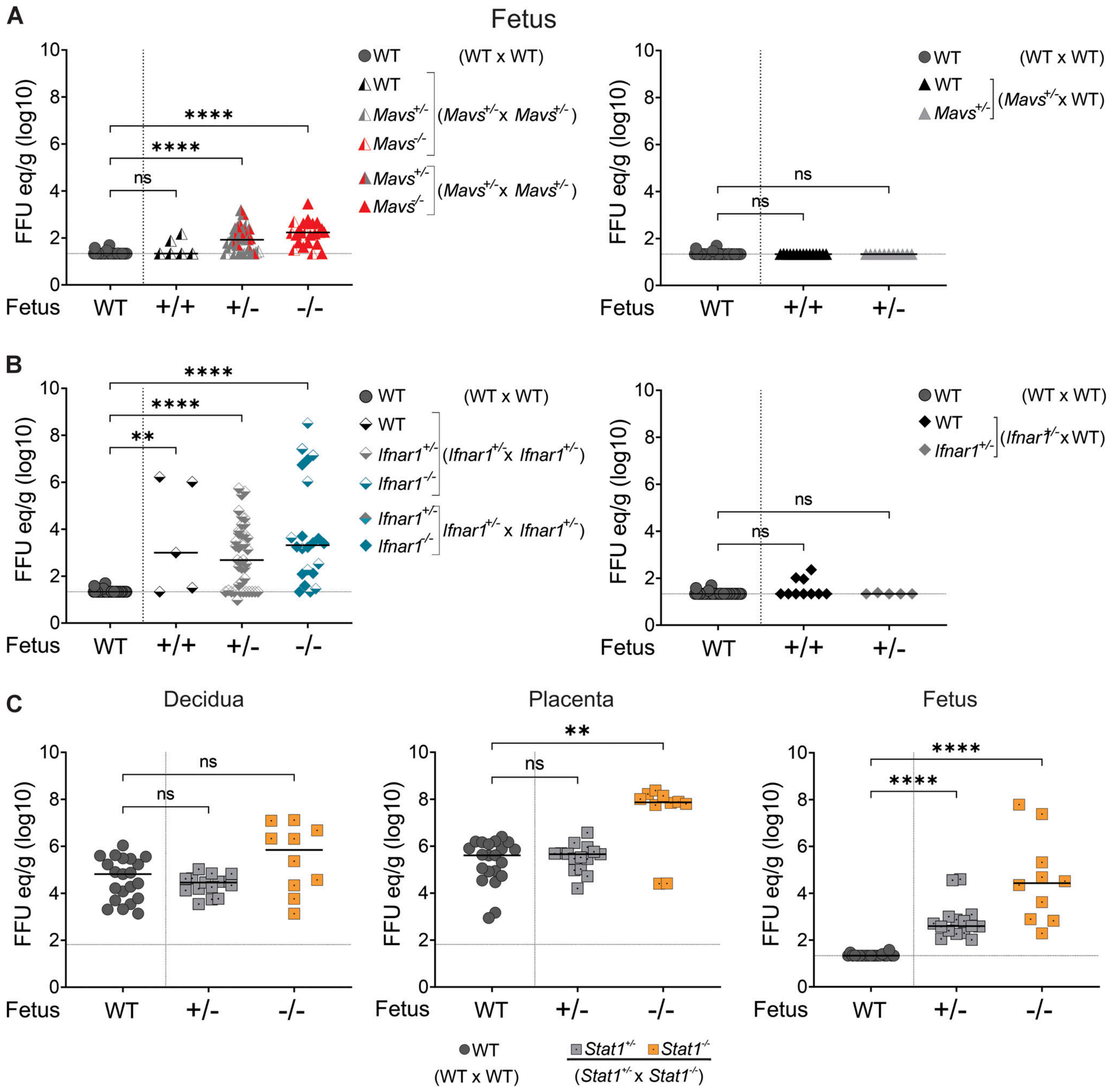

Figure 4. **MAVS and type I IFN signaling restrict ZIKV infection in the fetus. (A and B)** Viral burden (ZIKV RNA) in fetuses from Fig. 3 experiment. For simplification, samples were grouped by fetal genotype, independent of the breeding scheme for the target genes (see Fig. 3 legend). Data are from three experiments, with samples pooled from *n* = 5 dams per group. **(C)** *Stat1*$^{+/-}$ females were mated with *Stat1*$^{-/-}$ males and inoculated via intravenous injection at E9.5 with 3.5 × 10^5 FFU of ZIKV. ZIKV RNA levels were measured at 8 dpi. Data are pooled from two experiments (*n* = 5 dams [WT × WT] and *n* = 2 dams [*Stat1*$^{+/-}$ × *Stat1*$^{-/-}$] per group). Statistical analysis: Kruskal–Wallis test with Dunn's post-test (comparison to samples from WT × WT matings; **P < 0.01, ****P < 0.0001, ns, not significant). Dotted horizontal lines represent the LOD.

snRNAseq analysis reveals cell-type-specific innate immune signaling programs

To gain more insight into the cell-type-specific responses against ZIKV infection at the maternal–fetal interface, we performed snRNAseq analysis on WT or *Mavs*$^{-/-}$ placentas and their corresponding deciduas from WT female × WT male crosses or *Mavs*$^{+/-}$ female × *Mavs*$^{-/-}$ male crosses. After intravenous inoculation with ZIKV or PBS (mock) at E9.5, we analyzed the transcriptional changes in WT and *Mavs*$^{-/-}$ placentas at E12.5 (3 dpi) and E15.5 (6 dpi). We used earlier time points for the snRNAseq experiment to maximize the number of viable placentas at the time of collection and allow for the detection of innate immune responses, which could occur preferentially at earlier stages of infection. Analysis of viral RNA in littermates confirmed greater viral burden in *Mavs*$^{-/-}$ placenta and adjacent decidua compared with WT controls (~10 and ~20 fold, respectively at 6 dpi; P < 0.0001; Fig. S4 A). We obtained 98,661 nuclei with a median of 3,077 genes detected per nucleus after

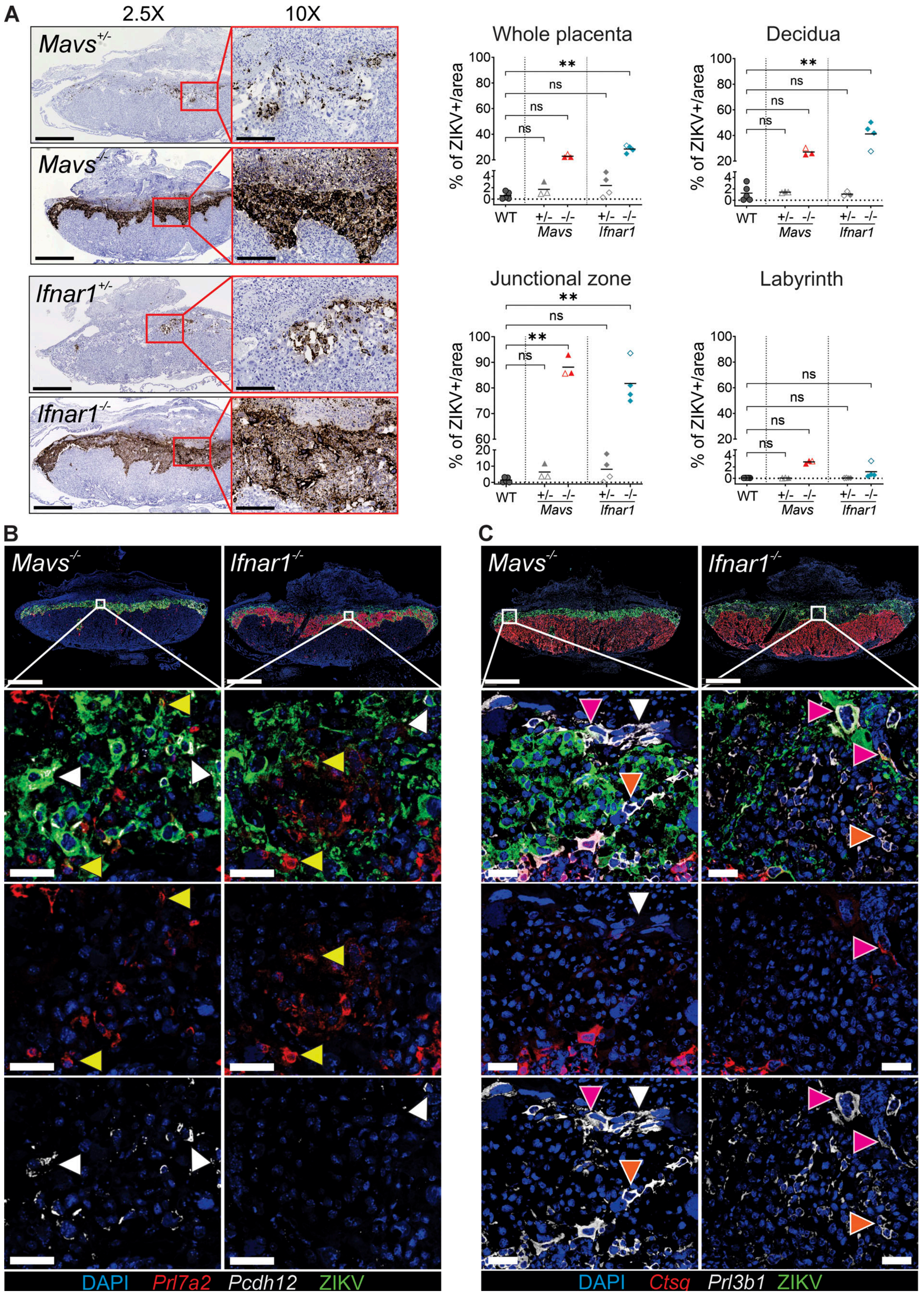

Figure 5. **Fetal MAVS and type I IFN signaling control ZIKV infection in the junctional zone of the placenta. (A)** Representative images of ZIKV RNA ISH in placentas homozygous or heterozygous for *Mavs* or *Ifnar1* gene deficiencies (left panel). Placenta images at 2.5× magnification (scale bars: 1 mm); insets at

10× magnification (scale bars: 250 µm). Quantification of ZIKV-positive areas as performed by semiautomated analysis using QuPath software (right panel). Each data point represents the average of at least two tissue sections from the same placenta (three to five placentas from at least two dams). Maternal decidua samples were grouped by the genotype of the corresponding fetus. Open symbols indicate samples from *Mavs*$^{+/-}$ × *Mavs*$^{+/-}$ and *Ifnar1*$^{+/-}$ × *Ifnar1*$^{+/-}$ crosses, shaded symbols are *Mavs*$^{+/-}$ × *Mavs*$^{-/-}$ and *Ifnar1*$^{+/-}$ × *Ifnar1*$^{-/-}$ crosses. Dotted horizontal lines represent the LOD of the assay. **(B and C)** Representative images of multiplex FISH for ZIKV, *Prl7a2*, and *Pcdh12* RNA (B), or for ZIKV, *Ctsq*, and *Prl3b1* RNA (C) in *Mavs*$^{-/-}$ or *Ifnar1*$^{-/-}$ placentas at 8 dpi. Placenta images at 2.5× magnification (scale bars: 1 mm); insets are maximum projection of three to four confocal z-stacks taken at 20× magnification (scale bars: 50 µm). **(B)** White arrowheads, GlyC; yellow arrowheads, SpT. **(C)** White arrowheads, ZIKV^{-} P-TGC; magenta arrowheads, ZIKV^{+} P-TGC; orange arrowheads, SpT. Images are representative of two experiments, $n = 2$ dams per group. Statistical analysis: (A) Kruskal–Wallis ANOVA with Dunn's post-test (comparison to WT tissues from WT × WT matings; $^{**}P < 0.01$, ns, not significant).

data processing and quality control (see Materials and methods). Seurat integrated analysis (Haghverdi et al., 2018; Stuart et al., 2019) and graph-based clustering identified cell types in maternal and fetal compartments based on analysis of canonical cellular markers (Fig. S4, B–D; see Materials and methods). Cell clusters derived from the dam included decidual stromal cells (Dec-Str), immune cells (Mat-Imm), and endothelial cells (Mat-Endot), among others (see Materials and methods). We also identified cell types in the fetal placental compartment, including the main trophoblast subtypes from the junctional zone (SpT, GlyCs, and junctional zone precursors [JZP]) and the labyrinth zone (labyrinth precursors, SynT [SynTI and SynTII], endothelial cells [Fetal-Endot], and S-TGC) (Fig. 7 A and Fig. S4 D). While we detected a small population of *Ptprc*$^{+}$/*Lyz2*$^{+}$ cells (Fig. S4, C–E, Mix-Imm) that could represent placental fetal macrophages, this cluster exhibits a mixed expression of *Xist* and *Ddx3y* and thus may include cells of maternal origin. Nevertheless, very few cells were detected for this cluster at any given condition (<20 cells per sample, Fig. S4 E), reflecting their low abundance in the murine placenta (Freyer et al., 2022).

We focused our analysis on ZIKV-induced transcriptional responses at 6 dpi (E15.5), as most of the differentially expressed genes were upregulated at this time point compared with 3 dpi (Fig. 7 B). We selected specific cell clusters that were permissive for infection (see Fig. 5 and Fig. S3 A) and/or showed greater changes in gene expression (Fig. 7 B). Hallmark pathway enrichment analysis revealed that at 6 dpi, pathways related to immune responses were upregulated in all clusters from both genotypes, except for the SpTs of *Mavs*$^{-/-}$ placentas, which showed a reduced enrichment of genes related to IFN and other immune responses, including IFN-α and IFN-γ pathways (Fig. S4 F). We next analyzed the expression of several ISGs and VSGs that were among the most upregulated genes at 6 dpi after ZIKV infection (Fig. 7 C and GEO accession GSE269612). In the maternal compartment of uninfected animals, baseline ISG expression was comparably low between WT or *Mavs*$^{+/-}$ deciduas (Fig. 8 A, left panel). ZIKV infection induced expression of RLRs (*Ddx58/Rig-I*, *Ifih1/Mda5*), genes downstream of IFNAR signaling (*Stat1*, *Stat2*), and antiviral signaling genes (*Ifit1*, *Ifitm3*, *Oasl2*, *Rsad2*) in Mat-Imm and Mat-Endot cells, and to a lesser extent in decidual stroma, whereas chemokine expression was observed principally in Mat-Imm cells (Fig. 8 A, left panel, and Fig. 7 C). To corroborate our cell-type-specific analyses, we validated *Rsad2* and *Ifit1* expression through an orthogonal imaging approach; these genes were selected due to their high expression across different cell clusters and because they represent MAVS-dependent or MAVS-independent ISGs in specific cell types. FISH analysis of samples collected at 8 dpi confirmed ZIKV-induced expression of *Rsad2* and *Ifit1* in *CD31 (Pecam1)*$^{+}$ decidual endothelial cells, *CD45 (Ptprc)*$^{+}$ decidual immune cells, and vimentin (*Vim*)$^{+}$ Dec-Str cells (Fig. 8 B, insets 1 and 3, Fig. 8 C, and Fig. 9 A), and this pattern was independent of the fetal genotype.

In the fetal placenta, our snRNAseq analysis showed that the responses to ZIKV infection varied by cell type and genotype (Fig. 8 A, right panel, and Fig. S5 A). GlyCs of both WT and *Mavs*$^{-/-}$ placentas showed upregulation of several ISGs at 6 dpi, including those related to RLR expression and function (*Ddx58/Rig-I*, *Ddx60* and *Ifih1/Mda5*), IFN induction and signaling (*Irf7*, *Stat1*, and *Stat2*), and antiviral effector activities (*Oasl2*, *Ifit1*, *Ifit2*, *Ifit3*, and *Rsad2* [viperin]), although the magnitude of the response trended lower in *Mavs*$^{-/-}$ cells (Fig. 7 D and Fig. 8 A, right panel). FISH analysis at 8 dpi showed that *Rsad2* and *Ifit1* colocalized with *Pcdh12*$^{+}$ GlyCs in the junctional zone and those invading the decidua in WT placentas, whereas in *Mavs*$^{-/-}$ placentas, *Rsad2* expression was detected only in invasive GlyCs (Fig. 9, A and B). Our transcriptomic analysis showed that host defense responses were more MAVS-dependent in SpTs, including upregulation of *Ddx60*, *Rsad2*, *Usp18*, *Ifih1*, *Isg15*, and *Irf7* (Fig. 7 D, Fig. 8 A, right panel, and Fig. S5 A). Indeed, *Rsad2* expression was increased in the junctional zone of ZIKV-infected WT but not *Mavs*$^{-/-}$ placentas (Fig. 9 C). Within the junctional zone of WT placentas, *Rsad2* colocalized with some CK7^{+} P-TGCs (Fig. 9 D, insets 1 and 3), and with *Prl7a2*$^{+}$ SpTs (Fig. 9 E, insets 1 and 3), but this pattern was not observed in *Mavs*$^{-/-}$ placentas. In the labyrinth zone, which was relatively resistant to ZIKV infection, there was a limited host defense response in S-TGCs and SynTII cells, which was generally independent of MAVS signaling. In comparison, expression of several RLR-related and IFNAR signaling genes was upregulated in SynTI cells, from either WT or *Mavs*$^{-/-}$ placentas after ZIKV infection (Fig. 8 A, right panel). Also, in fetal endothelial cells, we observed higher baseline and virus-induced expression of several ISGs, including *Rsad2*, *Ifit1*, *Trim30a*, and *Oasl2*, and this was independent of the genotype (Fig. 8 A, right panel). FISH analysis confirmed that the expression of *Rsad2* after ZIKV infection was principally restricted to vimentin^{+}/*CD31 (Pecam1)*$^{+}$ fetoplacental endothelial cells in both WT and *Mavs*$^{-/-}$ placentas at 8 dpi (Fig. 8 B and Fig. 9 D; in both insets 2 and 4) and was not detected in syncytial cells (CK7^{+}) or S-TGC (*Ctsq*$^{+}$) (Fig. 9, D and E, insets 2 and 4). Thus, only some cells (e.g., SpTs) required MAVS signaling pathways to express certain ISGs after ZIKV infection. Taken together, these data suggest that, in the fetal placenta, there are cell-type-specific MAVS-dependent

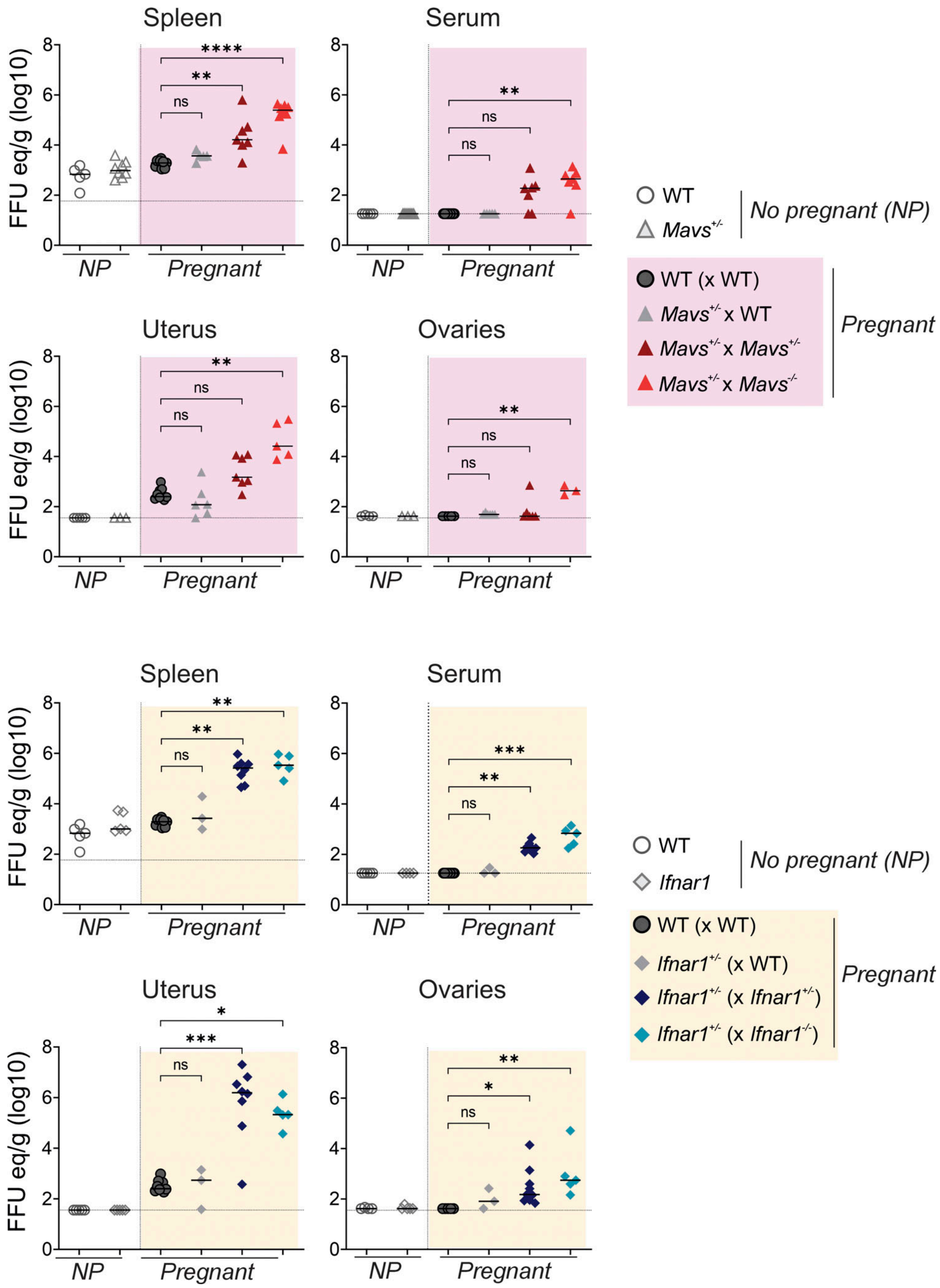

Figure 6. **MAVS and type I IFN signaling in the placenta limit maternal infection.** ZIKV RNA levels at 8 dpi in tissues from non-pregnant WT, *Mavs*$^{+/-}$, and *Ifnar1*$^{+/-}$ females and pregnant WT, *Mavs*$^{+/-}$, and *Ifnar1*$^{+/-}$ dams mated with indicated males. Data are from three experiments, with n = 5–9 or 3–8 dams per group (top and bottom panels, respectively). Statistical analysis: Kruskal–Wallis ANOVA with Dunn's post-test (comparison to WT dams crossed to WT sires; $^{*}P < 0.05$, $^{**}P < 0.01$, $^{***}P < 0.001$, $^{****}P < 0.0001$, ns, not significant). Dotted horizontal lines represent the LOD.

and MAVS-independent mechanisms to express ISGs at baseline or after ZIKV infection.

As some of the MAVS-dependent induction pathways might depend on IFNAR1, we analyzed expression of *Rsad2* and *Ifit1* at 8 dpi in *Ifnar1*$^{-/-}$ placentas by FISH and immunofluorescence microscopy. Compared with WT and *Mavs*$^{-/-}$ placentas, *Rsad2* and *Ifit1* expression was present more diffusely in *Ifnar1*$^{-/-}$ placentas (Fig. 9 C and Fig. 10, A and E). *Rsad2* expression was detected in some SpTs and P-TGCs of *Ifnar1*$^{-/-}$ placentas upon ZIKV infection (Fig. 10 B), which suggests a MAVS-dependent, IFNAR1-independent induction of *Rsad2* in these cells. ZIKV-induced expression of *Rsad2* in the fetal endothelium was independent of IFNAR1 expression as well, as it was detected in *Ifnar1*$^{-/-}$ vimentin^{+} cells (Fig. 10 C). However, and distinct from WT or *Mavs*$^{-/-}$ infected samples, *Rsad2* expression was increased in syncytial cells (CK7^{+}) and S-TGC (*Ctsq*$^{+}$) of *Ifnar1*$^{-/-}$ infected placentas (Fig. 10 D), indicating the existence of an IFNAR1-independent antiviral mechanism in these cells. Indeed, *Ifit1*

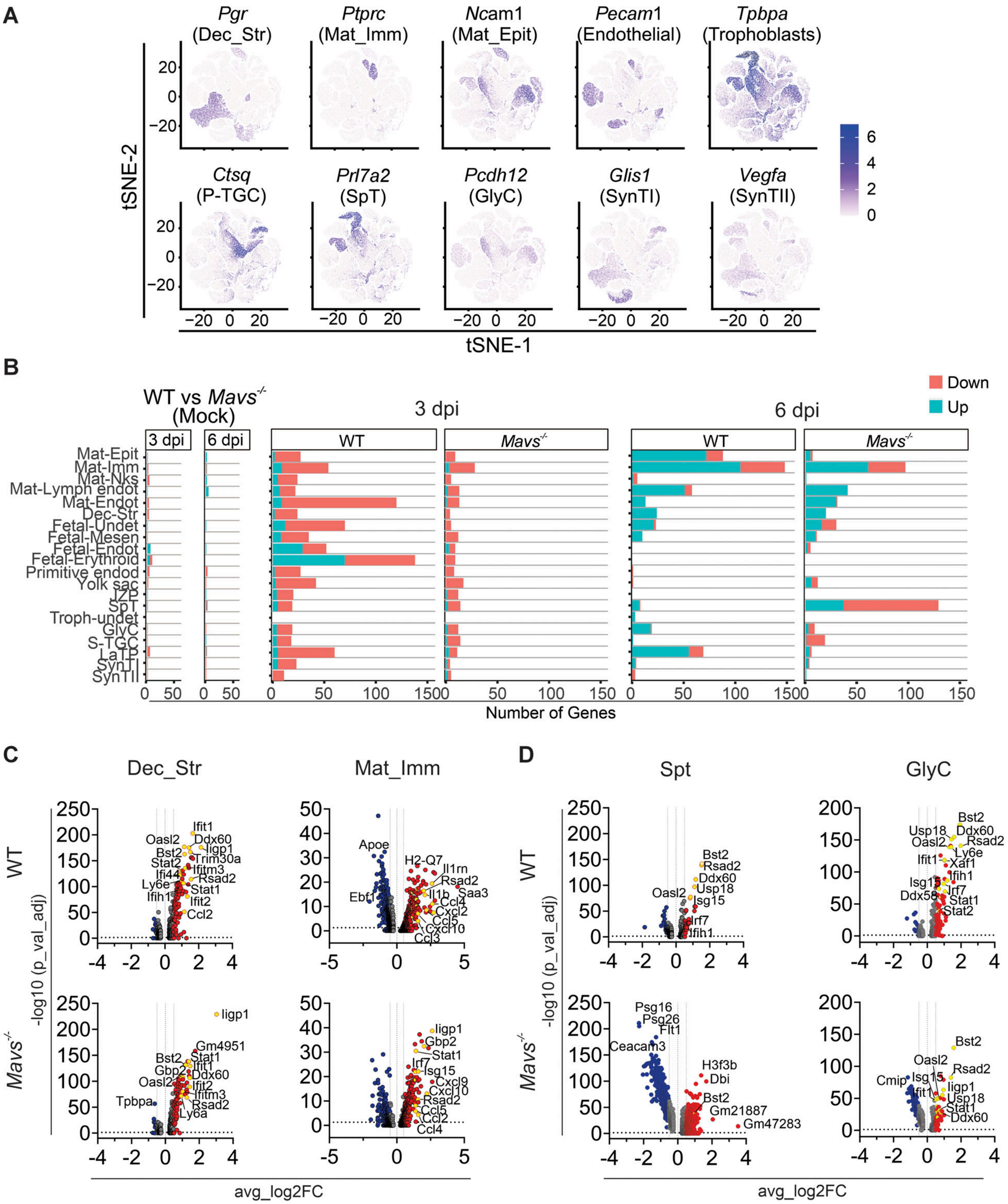

Figure 7. **snRNAseq of WT and *Mavs*$^{-/-}$ placentas reveals cell-type-specific innate immune responses. (A)** Expression of genes unique to maternal Dec-Str (*Pgr*), immune cells (*Ptprc*), endothelial cells (*Pecam*), pan-trophoblast (*Tpbpa*), GlyC (*Ncam1* and *Pchd12*), SpT (*Prl7a2*), TGC (*Ctsq*), and the SynT populations, SynTI (*Glis1*) and SynTII (*Vegfa*). **(B)** Bar plot showing the number of differentially expressed genes ($\log_2$ fold change [FC] > 1 and P < 0.05) in mock WT versus *Mavs*$^{-/-}$ placentas at E12.5 and E15.5 (left panel) and in ZIKV-infected WT and *Mavs*$^{-/-}$ placenta (versus mock counterparts) at 3 and 6 dpi (middle and right panels, respectively). LaTP, labyrinth precursors. **(C and D)** Volcano plots of maternal (C) and fetal (D) selected clusters of infected WT and *Mavs*$^{-/-}$ placentas and their corresponding deciduas compared with mock-infected samples. Grey symbols represent changes <0.25 $\log_2$ FC; blue and red symbols represent changes >0.5 and <−0.5 $\log_2$ FC, respectively; yellow symbols denote some of the selected ISGs. The FDR was calculated by the Bonferroni correction method, and significant genes were set as those with FDR of <0.05, expressed as −log10 (p_val_adj); dots below the horizontal dotted line are non-significant. Two littermate placentas of male fetuses of each genotype and condition were pooled together for snRNAseq analysis.

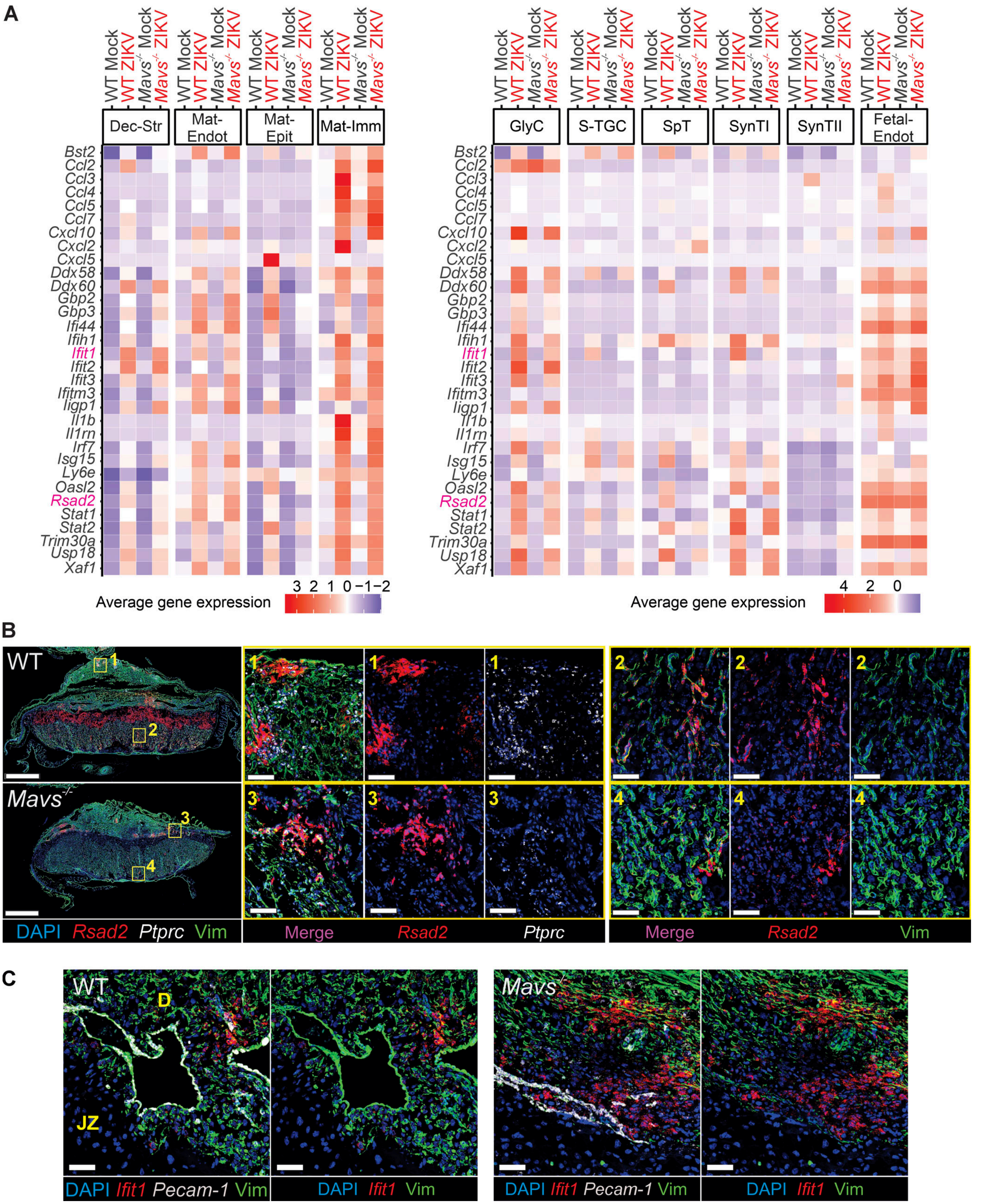

Figure 8. **Antiviral signaling in the maternal decidua is largely independent of fetal MAVS. (A)** Average gene expression of selected ISGs and VSGs in particular clusters of mock- and ZIKV-infected WT and *Mavs*$^{-/-}$ deciduas (right) and placentas (left). Genes selected for validation are shown in purple. **(B)** Representative images of multiplexed FISH for *Rsad2* and *CD45* (*Ptprc*) RNA combined with immunofluorescence for vimentin in WT and *Mavs*$^{-/-}$ placentas at 8 dpi. Placenta images at 2.5× magnification (scale bars: 1 mm); insets are the maximum projection of three to four confocal Z-stacks taken at 20× magnification (scale bars: 50 µm); numbers indicate the corresponding inset. **(C)** FISH for *Ifit1* and *CD31* (*Pecam-1*) combined with immunofluorescence for

vimentin in the decidua of ZIKV-infected WT and *Mavs*$^{-/-}$ placentas. Images of junctional zone (JZ) and decidua (D) at 20× magnification (maximum projection of three to four confocal z-stacks; scale bars: 50 μm). **(B and C)** Data are representative of two placentas for each condition from two dams.

also was widely expressed in *Ifnar1*$^{-/-}$ infected placentas compared with WT and *Mavs*$^{-/-}$ placentas (Fig. 10 E). In the labyrinth zone, *Ifit1* expression was apparent in *Ifnar1*$^{-/-}$ syncytial cells, S-TGCs, and Fetal-Endot cells (Fig. 10, F and G), suggesting that a lack of IFNAR1 signaling in the fetal placenta might be compensated by alternative innate immune signaling pathways to express ISGs. Indeed, quantitative RT-PCR (qRT-PCR) analysis of tissue homogenates from WT and *Mavs*$^{-/-}$ bulk placentas and corresponding deciduas showed comparable expression of ZIKV-induced genes (Fig. S5, B and C), which is consistent with the observation that MAVS-dependent signaling after ZIKV infection is restricted to a few cell types in the fetal placenta, mainly SpTs. Taken together, these results suggest that ZIKV infection can activate MAVS-dependent and IFNAR1-dependent, MAVS-dependent and IFNAR1-independent, or MAVS-independent and IFNAR1-dependent signaling pathways to induce ISGs and VSGs in different cells of the junctional and labyrinth zones, which influences viral tropism and burden.

Discussion

Our results show that in the setting of maternal immunocompetence, MAVS and IFNAR1 signaling pathways in the fetal compartment of the placenta control ZIKV tropism at the maternal–fetal interface, limit viral spread to the fetus, and prevent sustained viremia in the dam. Our data are consistent with studies showing increased infection in *Ifnar1*$^{-/-}$ placentas and fetuses compared with *Ifnar1*$^{+/-}$ littermates in a context of maternal IFNAR1 deficiency (Yockey et al., 2018), and establish that viral innate immune sensing via MAVS in the fetal placenta occurs independently of the dam. Our experiments also suggest that immune responses in the junctional zone depend on MAVS and type I IFN signaling pathways, which restrict ZIKV infection in SpTs and P-TGCs and prevent viral spread to the fetus and spillover back to the decidua. In comparison, MAVS- and IFNAR1-independent antiviral responses occur in other placental cell types, including fetoplacental endothelial cells and syncytial trophoblasts, which are less susceptible to ZIKV infection.

Mouse models with dams lacking IFNAR1 have been utilized to achieve placental and fetal ZIKV infection (Miner et al., 2016; Yockey et al., 2018). However, elevated viral burden in the dam and higher levels of maternally produced proinflammatory cytokines complicate the analysis of responses in the fetal compartment. As intravenous inoculation of ZIKV in immunocompetent dams can largely bypass restriction by peripheral maternal responses, yet still cause decidual and placental infection (Cugola et al., 2016; Szaba et al., 2018), we used this approach along with specific breeding schemes to study how innate immune pathways in the fetal compartment of the placenta impact vertical transmission in the context of intact maternal immune responses. Intravenous inoculation of ZIKV in WT dams mated to WT sires resulted in placental infection, injury, and inflammation, and in some instances, fetal growth restriction and demise, as described by others (Cugola et al., 2016; Szaba et al., 2018; Vermillion et al., 2017). Although some have reported more severe fetal outcomes (Szaba et al., 2018), the selection of virus or mouse strain may account for such differences (Bohm et al., 2021; Carbaugh et al., 2020). We evaluated ZIKV tropism in the fetal compartment of the placenta, which is comprised of different trophoblast subtypes, fetal immune cells, and endothelial cells, and in the maternal decidua, which is derived from the uterine endometrium. The fetal placenta provided a replicative niche for ZIKV, as viral RNA increased over time in this compartment. Moreover, ISH showed that ZIKV preferentially targeted mononuclear trophoblasts in the junctional zone (SpTs, P-TGCs, and GlyCs) compared with the more resistant S-TGCs, SynTs, and endothelial cells in the labyrinth zone, and the lower levels of infection in the maternal decidua. These findings are consistent with previous work showing higher levels of ZIKV infection in mononuclear trophoblasts of the junctional layer in *Ifnar1*$^{-/-}$ dams (Miner et al., 2016) and data from human samples suggesting greater ZIKV susceptibility of mononuclear cytotrophoblasts than SynT and decidual cells (Sheridan et al., 2017; Tabata et al., 2018; Tabata et al., 2016). Notwithstanding these results, others have reported ZIKV infection in fetal endothelial cells and SynTs in a model of intrauterine ZIKV infection in immunocompetent dams (Vermillion et al., 2017) and in samples from term placentas of ZIKV-infected patients (Rabelo et al., 2020). Furthermore, although human placental fetal macrophages have been described as possible ZIKV targets (Jurado et al., 2016; Quicke et al., 2016; Simoni et al., 2017; Zimmerman et al., 2018), we observed few CD45^{+} or CD11b^{+} cells in the mouse fetal placenta, and they could not be clearly identified in our snRNAseq analysis. Nonetheless, the cytokine signaling detected in the fetal compartment of the placenta also might reflect paracrine signals from immune cells at the maternal interface. Consistent with this idea, our snRNAseq data showed higher levels of cytokine and chemokine RNA in the Mat-Imm cell compartment. Disparities in susceptible cell types may reflect differences in experimental approach, gestational stage at the time of infection, or the species studied.

Single-cell sequencing approaches have helped to identify and characterize the distinct placental cell populations in humans and mice (Chen et al., 2023; Han et al., 2018; Jiang et al., 2023; Marsh and Blelloch, 2020; Nelson et al., 2016; Zhou et al., 2021). Differential cell responses to viral infection have been observed in human placenta samples and organoids (Ashary et al., 2020; Barrozo et al., 2023a; Wu et al., 2023), and in a gnotobiotic mouse model of ZIKV infection, where immune responses were identified in distinct placental microenvironments (Barrozo et al., 2023b). We compared cell susceptibility to ZIKV infection with transcriptional responses and cell-specific innate immune pathways by combining directed breeding schemes, ISH, immunofluorescence microscopy, and snRNAseq analysis. Although the involvement of type I IFN signaling in the control

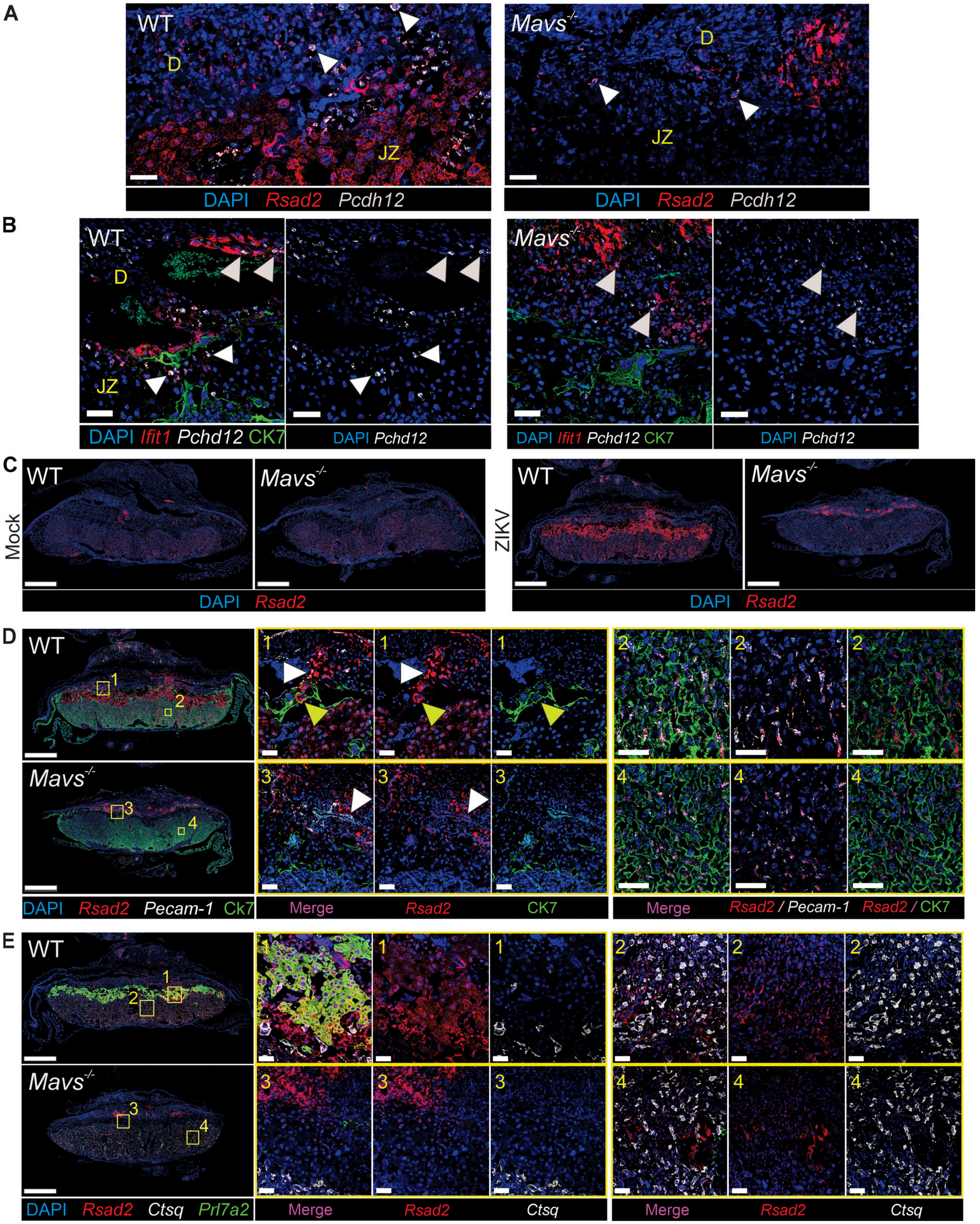

Figure 9. **ZIKV infection induces cell-specific expression of ISGs in the fetal compartment of the placenta. (A)** FISH for *Rsad2* and *Pcdh12* in infected deciduas adjacent to *Mavs*$^{-/-}$ placentas. **(B)** FISH for *Ifit1* and *Pcdh12* combined with immunofluorescence for CK7 in the junctional zone and decidua of ZIKV-infected WT and *Mavs*$^{-/-}$ placentas. **(C)** FISH for *Rsad2* RNA in WT and *Mavs*$^{-/-}$ placentas. **(D)** FISH for *Rsad2* and *CD31 (Pecam-1)* RNA combined with immunofluorescence for CK7 in WT and *Mavs*$^{-/-}$ placentas; white arrowheads, Mat-Endot cells; yellow arrowheads, P-TGC; numbers indicate the corresponding

inset. **(E)** Representative images of multiplexed FISH for *Rsad2*, *Prl7a2*, and *Ctsq* RNA in WT and *Mavs*$^{-/-}$ placentas. **(A and B)** Images of junctional zone and decidua at 20× magnification (maximum projection of three to four confocal z-stacks; scale bars: 50 µm); white arrowheads, *Rsad2* and *Ifit1*-expressing GlyCs. **(C–E)** Whole placenta images at 2.5× magnification (scale bars: 1 mm); insets in D and E are maximum projections of three to four confocal z-stacks taken at 20× magnification (scale bars: 50 µm). **(C and D)** Images of ZIKV-infected WT placentas are consecutive sections from the same placenta shown in Fig. 8 B. **(A–E)** Data are representative of two placentas for each condition from two dams collected at E17.5/8 dpi. D, decidua; JZ, junctional zone.

---

of ZIKV infection during pregnancy has been described in animal models (Miner et al., 2016; Yockey et al., 2016, 2018), it has not been clear which innate immune responses are most relevant in the fetal compartment in a setting of maternal immunocompetence. While viral sensing via RIG-I/MDA5-MAVS has been shown to restrict ZIKV infection in human placental cell lines (Ma et al., 2018; Zhao et al., 2022), this pathway has not been studied *in vivo*; however, deletion of the downstream transcription factors *Irf3* and *Irf7* facilitated placental and fetal infection in a mouse model of intravaginal ZIKV infection during pregnancy (Yockey et al., 2016). Our breeding schemes with immunocompetent (heterozygous) dams and immunocompetent (heterozygous) or immunodeficient (homozygous) sires enabled the generation of innate immune deficiencies specifically in the fetus. This allowed us to identify key roles for MAVS and IFNAR1 signaling but not other selected innate immune sensors or signaling molecules in the fetal placenta.

The deletion of fetal *Mavs* or *Ifnar1* resulted in widespread infection in the junctional zone. This suggests that the cells in the junctional zone rely on IFNAR1 signaling downstream of viral sensing via MAVS to limit ZIKV infection. ZIKV RNA appeared more abundant in the SpTs of *Mavs*$^{-/-}$ than *Ifnar1*$^{-/-}$ placentas, whereas the reverse was observed in P-TGCs, suggesting that MAVS and IFNAR1 pathways might act independently in these two cell types of the junctional layer to restrict ZIKV infection. Moreover, ZIKV RNA was sporadically detected in the fetoplacental endothelial cells in the labyrinth zone and fetal head of *Ifnar1*$^{-/-}$ but not *Mavs*$^{-/-}$ fetuses, suggesting that other viral sensors contribute to type I IFN signaling in cells of these compartments. MAVS is downstream of viral RNA sensing by cytosolic RLRs (such as RIG-I and MDA5) and can activate distinct antiviral pathways depending on the cell type (e.g., type I and III IFNs), some of which overlap but do not completely match IFNAR1 signaling (Lazear et al., 2019). FISH analysis of *Rsad2* mRNA, which can be stimulated through IFN-dependent or independent pathways (Ashley et al., 2019; DeFilippis et al., 2006; Rivera-Serrano et al., 2020; Stirnweiss et al., 2010), showed upregulation in SpTs and P-TGCs of *Ifnar1*$^{-/-}$ placentas after ZIKV infection but not in *Mavs*$^{-/-}$ placentas. Thus, different innate host defense response pathways may be utilized by distinct placental cell types. Indeed, our snRNAseq analysis revealed cell-type-specific antiviral responses after ZIKV infection. Cells in the junctional zone (SpT and GlyC) that were highly permissive for ZIKV infection upregulated different sets of ISGs. The actions of MAVS signaling were more restricted to SpTs, as certain ISGs and VSGs (e.g., *Rsad2*, *Isg15*, *Oasl2*, and *Usp18*) were induced in WT but not *Mavs*$^{-/-}$ cells after ZIKV infection. In contrast, the GlyCs expressed these and other ISGs after ZIKV infection independently of MAVS signaling. Our results suggest that MAVS-dependent sensing pathways direct antiviral signaling in SpT independently of IFNAR1, whereas antiviral responses in other cell types are regulated by MAVS and IFNAR1 signaling or alternative pathogen recognition receptors and IFNAR1 signaling pathways.

In the SynT and S-TGCs of the labyrinth zone, we also detected MAVS-independent and IFNAR1-independent induction of ISGs by snRNAseq and/or FISH. Fetal endothelial cells in the labyrinth zone also expressed a range of ISGs basally, independently of ZIKV infection or MAVS signaling. Although further studies are warranted, constitutive antiviral gene expression in the fetal endothelium, which underlies the SynT layer, might account for restriction of ZIKV infection in the labyrinth zone. We did not find evidence of global antiviral actions for TLR7, TLR9, MyD88, or STING signaling in the fetal placenta, although tropism and ISG expression analyses were not performed. Because the fetal viral burden in mice lacking STAT1 or IFNAR1 in the placenta is similarly increased, type I IFN–STAT1 signaling axis likely has a principal role in controlling ZIKV infection in the fetal compartment. However, future studies will be needed to assess roles for other antiviral pathways that use STAT1, including type II IFN-γ signaling, which can compensate for the loss of type I signaling and induce expression of ISGs (Lee and Ashkar, 2018). In human placentas, the constitutive secretion of type III IFN by SynTs has been proposed to prevent viral infection in these and other human cells at the maternal–fetal barrier (Ander et al., 2019). However, as recently shown (Casazza et al., 2022), we did not find evidence that fetal IFN-λ signaling in mice restricts placental infection at the stage of pregnancy that we examined. Overall, our results suggest that MAVS and type I IFN signaling in SpT and P-TGCs can affect viral spread within the junctional zone, whereas alternative host defense pathways might act in other cell types to prevent infection of labyrinth zone cells.

A prior study of congenital ZIKV infection in mice suggested that type I IFN signaling in the fetal placenta could promote fetal demise (Yockey et al., 2018). In that study, as we observed, ZIKV replicated to higher levels in *Ifnar1*$^{-/-}$ compared to *Ifnar1*$^{+/-}$ placentas. Whereas Yockey et al. (2018) observed that *Ifnar1*$^{+/-}$ fetuses were resorbed at a greater rate than *Ifnar1*$^{-/-}$ fetuses after ZIKV infection, we did not detect effects on fetal viability in the context of fetal type I IFN or MAVS signaling deficiencies. The following experimental differences that could explain this discrepancy: (i) we inoculated mice with ZIKV at mid-gestational age (E9.5) after placentation was established, whereas Yockey et al. (2018) inoculated dams at E5.5 prior to placentation; (ii) we used *Ifnar1*$^{+/-}$ dams, in contrast to the *Ifnar1*$^{-/-}$ dams used by Yockey et al. (2018). A deficiency of IFNAR1 in the dam likely results in greater maternal ZIKV infection, and high and sustained levels of type I IFN in maternal circulation, which could trigger sustained IFNAR1 signaling in

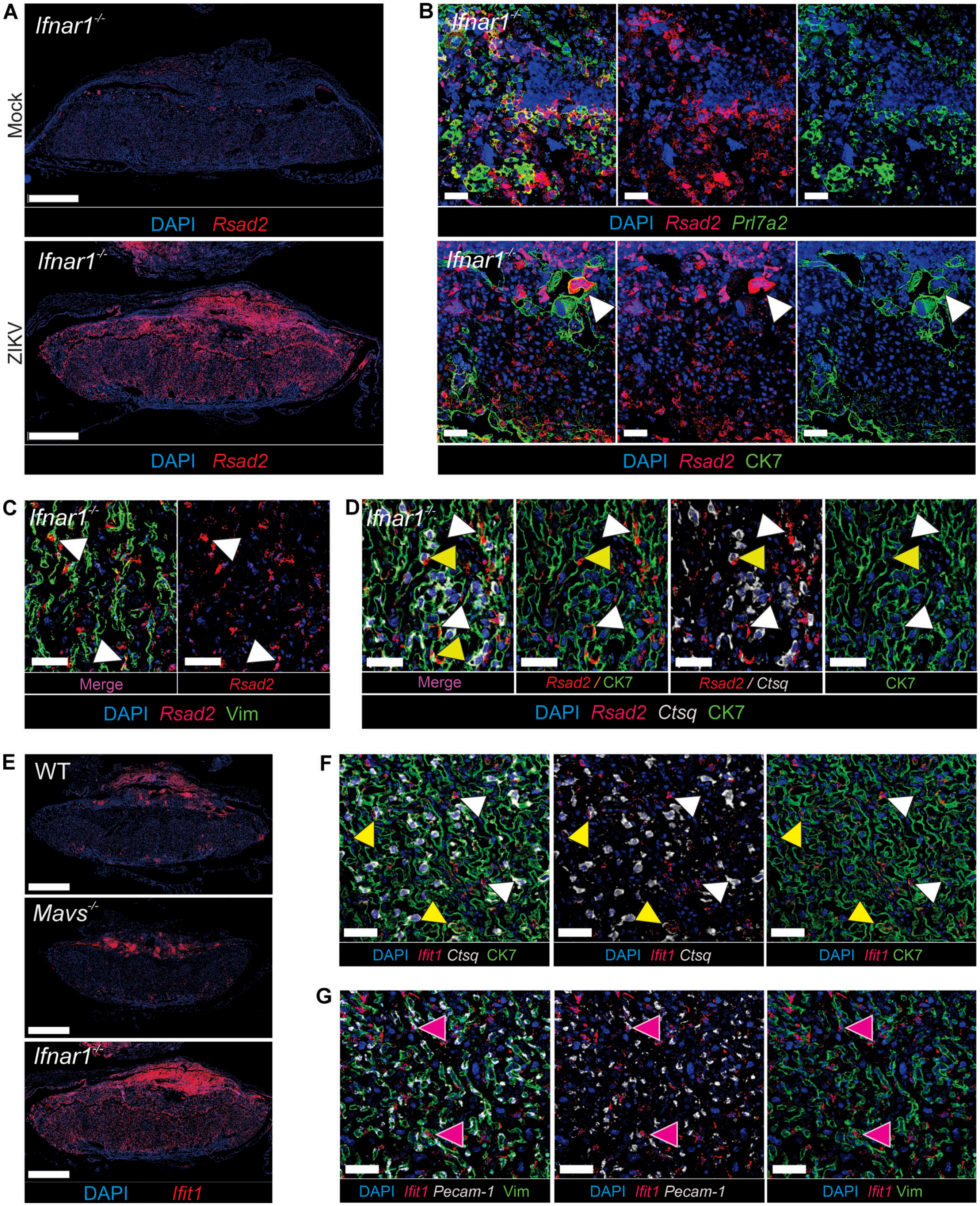

Figure 10. **ZIKV infection induces cell-specific expression of ISGs independent of IFNAR1 signaling. (A)** FISH for *Rsad2* RNA in mock- and ZIKV-infected *Ifnar1*$^{-/-}$ placentas. **(B)** FISH for *Rsad2* and *Prla7a2* RNA (top panel) and FISH for *Rsad2* combined with immunofluorescence for CK7 (bottom panel) in *Ifnar1*$^{-/-}$ ZIKV-infected placentas; white arrowheads denote *Rsad2* staining in P-TGC. **(C)** FISH for *Rsad2* combined with immunofluorescence for vimentin in ZIKV-infected *Ifnar1*$^{-/-}$ placentas; white arrowheads, *Rsad2*-expressing endothelial cells. **(D)** FISH for *Rsad2* and *Ctsq* RNA combined with immunofluorescence for

CK7 in *Ifnar1*$^{-/-}$ ZIKV-infected placentas; white and yellow arrowheads indicate co-localization of *Rsad2* with syncytial cells and S-TGC, respectively. **(E)** FISH for *Ifit1* RNA in ZIKV-infected WT, *Mavs*$^{-/-}$, and *Ifnar1*$^{-/-}$ placentas. **(F)** FISH for *Ifit1* and *Ctsq* RNA combined with immunofluorescence for CK7 in *Ifnar1*$^{-/-}$ ZIKV-infected placentas; white and yellow arrowheads indicate co-localization of *Ifit1* with syncytial cells and S-TGC, respectively. **(G)** FISH for *Ifit1* and *CD31* (*Pecam-1*) RNA combined with immunofluorescence for vimentin in *Ifnar1*$^{-/-}$ ZIKV-infected placentas; magenta arrowheads, co-localization of *Ifit1* with endothelial cells. **(A and E)** Placenta images at 2.5× magnification (scale bars: 1 mm). **(B)** Images of placental junctional zone taken at 20× magnification (maximum projection of three to four confocal z-stacks; scale bars: 50 μm). **(C, D, F, and G)** Images of placental labyrinth zones at 20× magnification (maximum projection of three to four confocal z-stacks; scale bars: 50 μm). **(A–G)** Data are representative of two placentas for each condition from two separate dams.

Ifnar1$^{+/-}$ placentas, with adverse effects on fetal development; and (iii) we inoculated pregnant mice with an African ZIKV strain via an intravenous route, whereas Yockey et al. (2018) inoculated dams with an Asian ZIKV strain via an intravaginal route. More study is needed to address the effects on fetal outcomes of different ZIKV strains and inoculation routes.

While the mouse placenta recapitulates many aspects of human placental physiology, there are differences in structure and cellular composition between the two species (Ander et al., 2019). The mouse SpT and P-TGCs, two of the cell types susceptible to ZIKV infection in our model, resemble the human mononuclear cytotrophoblasts and extravillous trophoblasts, which reportedly have varying degrees of susceptibility to ZIKV infection, although the outcomes depend on the source of human placental cells (i.e., blastocyst-derived, or first trimester/term placenta isolates) (Karvas et al., 2022; Sheridan et al., 2017; Wu et al., 2023). The multinucleated SynT of both species are relatively resistant to ZIKV infection (Delorme-Axford et al., 2013; Jagger et al., 2017). Cell-type-specific antiviral signatures have been described in response to ZIKV in human trophoblast stem cells, SynT, and extravillous trophoblasts (Wu et al., 2023), as well as in decidual and trophoblast organoids in response to human cytomegalovirus infection (Wu et al., 2023; Yang et al., 2022). Our mouse model supports an intrinsic antiviral defense program in the fetal compartment of the placenta, with cell-specific innate immune responses influencing viral tropism at the maternal–fetal interface.

Heterozygote, immunologically intact dams bearing *Mavs*$^{-/-}$ or *Ifnar1*$^{-/-}$ fetuses sustained higher ZIKV viremia and viral loads in the spleen, uterus, and ovaries than those bearing immunocompetent fetuses. This suggests that ZIKV infection in the placenta can influence the course of infection in the pregnant host, which in turn might affect pregnancy outcomes. Indeed, intact IFNAR1 signaling in the fetus can protect *Ifnar1*$^{-/-}$ dams from mouse hepatitis virus (MHV68)–induced mortality (Racicot et al., 2017), supporting the idea that placental immune responses modulate the course of infection in the mother. In humans, while ZIKV viremia in non-pregnant females is detectable for only 5–7 days (Waggoner et al., 2016), persistent viremia is frequently observed during pregnancy (Brasil et al., 2016; Driggers et al., 2016; Suy et al., 2016), occurring in up to 40% of cases (Pomar et al., 2021). Although it is possible that the maternal hormonal and immune environment during pregnancy favors viral persistence, it has been proposed that the placenta may act as a replicative niche for persistent ZIKV infection (Bhatnagar et al., 2017; Villazana-Kretzer et al., 2022). Thus, impaired placental immune responses, due to congenital defects or viral escape mechanisms, could contribute to persistent maternal viremia. Further research also is needed to address whether such mechanisms are specific to ZIKV or affect pregnancy and fetal outcomes in the context of other pathogens. Moreover, due to the multiparous nature of mouse pregnancies, litter effects might exist, and the relative proportion of immunocompetent to immunodeficient placentas present in the same dam could influence viral burden. This limitation can be addressed in future studies using alternative models, such as transfer of immunodeficient embryos to immunocompetent dams.

In summary, our experiments suggest that MAVS and IFNAR1 signaling pathways in the fetal compartment can regulate vertical viral transmission, with intrinsic actions in the placenta and consequences on fetal and maternal infection and, possibly, disease outcome. While further investigations are required to address the alternative pathways that mediate responses to ZIKV and other pathogens, our findings highlight the importance and complexity of placental innate immunity in protecting the fetus from viral infection, as well as its influence on the pathogenesis in the pregnant host.

Materials and methods

Cells and viruses

Vero (ATCC CCL-81) cells were used for propagation and titering of ZIKV stocks by focus-forming assay and for ZIKV burden assessment by plaque assay. Cells were propagated in Dulbecco's Modified Eagle Medium (DMEM; #11995-040; Gibco) supplemented with 5% heat-inactivated FBS (#FB-01; Omega Scientific), 100 U/ml penicillin–streptomycin (#15140-122; Gibco), and 10 mM HEPES (#15630-080; Gibco). Cells were maintained at 37°C in the presence of 5% CO_2.

Mouse-adapted ZIKV Dakar 41525 was generated previously (Senegal, 1984; GenBank: KU955591.1) as described (Gorman et al., 2018) and encodes an additional NS4B-G18R point mutation.

Mice

Housing and care of laboratory animals was conducted in accordance with guidelines from the National Institutes of Health (NIH), Bethesda, MD, USA, Guide for the Care and Use of Laboratory Animals. Animal husbandry and experiments were performed in accordance with guidelines from the Institutional Animal Care and Use Committee at Washington University in St. Louis School of Medicine (Assurance number A3381-01). WT C57BL/6 mice (000664) were purchased from Jackson Laboratories and housed at least 2 wk before the experiments. *Stat1*$^{-/-}$, *Myd88*$^{-/-}$, *Tlr7*$^{-/-}$, *Tlr9*$^{-/-}$, and *Sting*$^{-/-}$ (Sting GT) mice were originally purchased from Jackson Laboratories (012606, 009088, 008380, 034329, and 017537, respectively). All the other mouse strains used were previously described (*Mavs*$^{-/-}$ [Kumar et al., 2006], *Ifnar1*$^{-/-}$ [Müller et al., 1994], and *Il28ra*$^{-/-}$ [Ank et al., 2008]). All mice were backcrossed onto a C57BL/6 background using speed congenics and single-nucleotide polymorphism analysis. For genotyping of adult mice and fetuses, ~1 mm^2 of mouse tail was digested in 75 µl of alkaline lysis buffer (25 mM NaOH and 0.2 mM EDTA, pH 12) for 15 min at 95°C and neutralized with 75 µl of neutralization buffer (40 mM Tris-HCl, pH 5). Samples were then clarified by centrifugation and used for in-house PCR (Table S1) or sent to a commercial vendor (Transnetyx) for further purification and qPCR analysis.

Breeding strategies

We crossed WT C57BL/6 female mice (000664; Jackson Laboratories) with males homozygous for deletions in key innate immune response genes to generate heterozygous females. The heterozygous females were mated with respective heterozygous or homozygous males to generate WT, heterozygous, and homozygous placentas. Of note, we combined data with a given genotype from different crosses to gain statistical power, although separate analyses of heterozygous × homozygous and heterozygous × heterozygous crosses confirmed similar trends. We also crossed WT or heterozygous females with WT males (000664; Jackson Laboratories) as controls to assess for possible effects of maternal haploinsufficiency.

In vivo infections

Timed pregnancies were set up, and E0.5 was determined after detecting vaginal plugs. Dams were inoculated at E9.5 with 3.5 × 10^4, 3.5 × 10^5, or 3.5 × 10^6 FFU of ZIKV (Dakar 41525 with NS4B-G18R [Gorman et al., 2018]) intravenously via retro-orbital route under isoflurane anesthesia. Dams were sacrificed at E11.5 (2 dpi), E12.5 (3 dpi), E13.5 (4 dpi), E15.5 (6 dpi), or E17.5 (8 dpi). Dams were evaluated for weight loss or lethargy throughout the course of infection.

qRT-PCR analysis of viral burden

Viral burden was measured in the decidua, placenta, fetus, and other maternal tissues (serum, spleen, uterus, and ovaries). The decidua was dissected from the fetal placenta as described before (Qu et al., 2014). Fetoplacental units were placed on ice-cold PBS in a Petri dish, the uterine tissue was carefully removed from each unit, and the decidua was peeled from the fetal placenta using fine tweezers. Fetal placenta was separated from the fetus by cutting the umbilical cord proximal to the chorionic plate. Decidual and placental tissues were placed immediately in prechilled 2-ml tubes, and fetuses were arranged on a prechilled tissue grid for photography and determination of fetal size before dissection of the fetal heads. Tissues were weighed and homogenized with zirconia beads using a MagNA Lyser (Roche LifeScience). Homogenates were clarified by centrifugation at 10,000 × *g* for 10 min, and RNA was extracted using the 5X MagMax Viral Isolation kit (Applied Biosystems) on a Kingfisher Flex extraction robot (Thermo Fisher Scientific). ZIKV RNA was reverse transcribed and amplified using the TaqMan RNA-to-CT 1-Step kit (Thermo Fisher Scientific). Reverse transcription was carried out on a QuantStudio 6 Flex System (Applied Biosystem) at 48°C for 15 min followed by 2 min at 95°C. Amplification was accomplished over 40 cycles as follows: 95°C for 15 s and 60°C for 1 min. RNA quantity was expressed as viral RNA equivalents per gram (tissue) or milliliter (serum) after interpolation onto a standard curve of 10-fold dilutions of ZIKV (Dakar 41525) RNA. The primer sets have been previously published (Gorman et al., 2018; Lazear et al., 2013).

Focus-forming assay

Virus titration was performed as previously described (Brien et al., 2013) with modifications. Vero cells were seeded in flat-bottom 96-well plates (TPP #92696) at 2 × 10^4 cells/well in a volume of 100 µl/well. The next day, virus stocks were serially diluted in infection media (DMEM with 2% heat-inactivated FBS, 100 U/ml penicillin–streptomycin, and 10 mM HEPES pH 7.3). 100 µl of the diluted samples were added to Vero cell monolayers and incubated for 1 h at 37°C in 5% CO_2. Subsequently, cells were overlaid with 100 µl of 1% methylcellulose in Minimum Essential Medium (Sigma-Aldrich #M0275 supplemented with 100 U/ml penicillin-streptomycin, 10 mM HEPES, pH 7.3, and 1 × GlutaMAX (Gibco #35050-061). Plates were fixed 40 h after virus inoculation with 100 µl of 1% paraformaldehyde (PFA; EMS #15713-S) in PBS for 1 h at room temperature. After three washes with PBS, samples were incubated on a plate rocker with 0.5 µg/ml of mouse anti-WNV E60 (flavivirus cross-reactive, Zhao et al., 2016) diluted in permeabilization buffer (PBS, 0.1% saponin [Sigma-Aldrich #S7900], and 0.1% bovine serum albumin [BSA; Sigma-Aldrich #A2153]) for 2 h at room temperature. Primary mAb was removed after three washes with PBS-T 0.05% (PBS with 0.05% Tween-20, Sigma-Aldrich #P1379), and samples were incubated with secondary peroxidase-conjugated goat anti-mouse IgG (Sigma-Aldrich #A5278) diluted 1:500 in permeabilization buffer for 1 h at room temperature on a rocker. After three washes with PBS-T 0.05%, virus-infected foci were developed using KPL TrueBlue peroxidase substrate (SeraCare #5510-0050), washed twice with Milli-Q water, and counted using a CTL-S6 Universal Analyzer (ImmunoSpot). Viral titers were expressed as FFU per milliliter.

Plaque assays

Vero cells were plated in 12-well culture dishes at 1.4 × 10^5 cells/well and incubated overnight at 37°C in DMEM supplemented with 10% FBS. Media was changed the next day to 2% FBS with penicillin/streptomycin (Gibco), and 75 µl of serially diluted (tenfold) clarified tissue homogenate or serum was added to the wells. After 1 h, cells were overlaid with methylcellulose and incubated for 4 days. Cells were fixed with 10% formaldehyde overnight and stained with crystal violet. Plaques were manually counted, and viral titers were expressed as PFU per gram of tissue or milliliter (serum).

Histology

Individual placentas (including the decidua) were collected at E17.5 from dams that were mock or ZIKV infected at E9.5, and samples were rinsed in PBS and fixed overnight in 4% PFA at room temperature. Samples were rehydrated in 70% ethanol and refrigerated until processing for paraffin embedding. Tissue was sagitally sliced with a microtome into serial 4-µm sections and mounted by the Washington University Musculoskeletal Histology and Morphometry Core. Sections were stained with hematoxylin (#H-3401; Vector) and eosin (#HT110132; Sigma-Aldrich) following standard procedures. Full placenta sections were scanned with a Hamamatsu NanoZoomer (HT) at 20× resolution. Measurements of placental areas were performed using QuPath software (Bankhead et al., 2017) using a semiautomatic approach in which placental regions, including the fetal compartment (labyrinth and junctional zones) and the proximal decidua, were manually drawn and annotated, and automatically measured by the software. Histopathological assessments were analyzed by a blinded investigator.

Immunofluorescence microscopy

Paraffin-embedded sections were deparaffined, washed three times with PBS, and antigen-retrieval was performed in boiling Target Retrieval Solution (#S1699; Dako) for 15 min. Samples were then washed three times with PBS-T (PBS with 0.1% Tween-20, Sigma-Aldrich #P1379) and blocked for 30 min at room temperature staining buffer (1% BSA, 2% goat serum, and 0.1% Triton in PBS) supplemented with anti-CD16/32 to block Fcγ receptor binding at 1/100 dilution (#101302; Biolegend). Primary antibodies (Table S2) were incubated overnight at 4°C in staining buffer at 1/200 dilution, washed three times with PBS-T, and incubated with secondary antibodies (Table S2) at 1/1,000 dilution in staining buffer for 1 h at room temperature. After four washes with PBS-T, samples were stained with Hoechst 33258 (H3569; Invitrogen) and mounted with ProLong Gold Antifade Mountant (P36930; Thermo Fisher Scientific). Placental sections were scanned with a Hamamatsu NanoZoomer (HT) at 20× resolution.

Viral RNA ISH

RNA ISH was performed using RNAscope 2.5 HD-Brown (#322310; Advanced Cell Diagnostics) according to the manufacturer's instructions. Briefly, formalin-fixed, paraffin-embedded tissue sections were baked for 60 min at 60°C, and endogenous peroxidases were quenched with H_2O_2 for 10 min at room temperature. Slides were then boiled for 15 min in RNAscope Target Retrieval Reagents and incubated for 30 min in RNAscope Protease Plus reagent prior to hybridization with *ZIKV* RNA probe (Table S2), signal amplification, and detection with 3,3′-Diaminobenzidine (DAB). Sections were counterstained with Gill's hematoxylin and visualized by brightfield microscopy. Full-placenta sections were scanned with a Hamamatsu NanoZoomer (HT) at 20× resolution, and quantification of ZIKV-positive areas was performed using QuPath software (v. 0.3.0). QuPath's pixel classifier was trained to semiquantitatively detect the number of ZIKV-positive (DAB^+) and -negative (DAB^-) pixels from specified placental regions of interest (e.g., whole placenta and decidual, junctional, and labyrinth zones). The classifier operated using an artificial neural network (artificial neural networks—multilayer perceptrons) on four channels (red, green, blue, and DAB). These channels had Gaussian, Laplacian of Gaussian, and Hessian determinant transformations applied to minimize the effects of image variation on pixel detection. To normalize ZIKV-positive and -negative pixel measurements across the regions of interest of different placental sections, the total number of pixels in a given area was measured to obtain the percentage of ZIKV-positive pixels.

Multiplexed FISH

Detection of multiple mRNA transcripts (Table S2) was performed using RNAscope Multiplex Fluorescent Reagent Kit v2 (#323100; Advanced Cell Diagnostics) following the manufacturer's instructions. Briefly, samples were processed as described in the "Viral RNA ISH" section above, and hybridization was performed using probes labeled with different fluorescence spectra. The signal was recorded sequentially using fluorophores assigned to each channel (Table S2), slides were counterstained with DAPI, and coverslips were mounted using ProLong Gold Antifade Mountant (P36930; Thermo Fisher Scientific). Full-placenta sections were scanned with a Hamamatsu NanoZoomer (HT) at 20× resolution. Some high-power images were captured using an LSM 880 confocal laser scanning microscope (Zeiss) at the Washington University Molecular Microbiology Imaging Facility at 20× (NA 0.8) objective. Z-steps were acquired through the entire tissue thickness (3–4 z-layers).

Multiplexed FISH combined with immunofluorescence

Codetection of RNA transcripts and proteins was performed using the Advanced Cell Diagnostics (ACD) Integrated RNAscope Multiplex Fluorescent v2 Assay combined with RNA-Protein Co-detection Ancillary Kit (#323180ACD) following the manufacturer's instructions. Briefly, samples were processed as described in the section "Viral RNA ISH" above, washed with PBS-T after antigen retrieval, and incubated with primary antibodies (Table S2) overnight at 4°C. Samples were then fixed again in 4% PFA/PBS before protease treatment, hybridization, and signal amplification, followed by incubation with fluorophore-conjugated secondary antibodies (Table S2) (30 min at room temperature). Slides were counterstained with DAPI and coverslips were mounted using ProLong Gold Antifade Mountant. Full-placenta sections were scanned with a Hamamatsu NanoZoomer (HT) at 20× resolution. Some high-power images were captured using an LSM 880 confocal laser scanning microscope (Zeiss) at the Washington University Molecular Microbiology Imaging Facility at 20× (NA 0.8) objective. Z-steps were acquired through the entire tissue thickness (3–4 z-layers).

Cytokine determination

Clarified homogenates from fetal placentas were incubated with Triton-X-100 (1% final concentration) for 1 h at room temperature to inactivate ZIKV. Homogenates were analyzed for cytokines and chemokines by Eve Technologies Corporation using their Mouse Cytokine Array/Chemokine Array 31-Plex (MD31) platform.

snRNAseq

WT dams mated with WT sires or $Mavs^{+/-}$ dams mated with $Mavs^{-/-}$ sires were mock or ZIKV infected (3.5×10^5 FFU), and placenta with their corresponding decidua were collected and snap-frozen in liquid nitrogen at 3 or 6 dpi. After genotyping, we selected placentas from male fetuses to facilitate the identification of maternal and fetal clusters and doublets. Two placentas from the same genotype and condition were pooled and processed for isolation of nuclei. Nuclear extraction was adapted from a previously described protocol for jejunal segments (Chang et al., 2024). Briefly, tissues were thawed and minced in lysis buffer (25 mM citric acid, 250 mM sucrose, 0.1% NP-40, and 1X protease inhibitor [Roche]). Nuclei were released from cells using a Dounce homogenizer (Wheaton) then washed three times with buffer (25 mM citric acid, 0.25 M sucrose, 1X protease inhibitor [Roche]), and then filtered successively through 100-, 70-, and 40-µm diameter strainers (pluriSelect) to obtain single nuclei in resuspension buffer (25 mM KCl, 3 mM $MgCl_2$, 50 mM Tris, 1 mM DTT, 0.4 U/µl RNase inhibitor [Sigma-Aldrich] and 0.4 U/µl Superase inhibitor [Thermo Fisher Scientific]). Approximately 10,000 nuclei per sample were subjected to gel bead-in-emulsion (GEM) generation, reverse transcription, and construction of libraries for sequencing according to the protocol provided in the 3′ gene expression v3.1 kit manual (10X Genomics). Briefly, cDNA was prepared after GEM generation and barcoding, followed by the GEM-RT reaction and bead cleanup steps. Purified cDNA was amplified for 11–13 cycles before clean-up using solid phase reversible immobilization beads (SPRI select beads, B23318; Beckman Coulter). Samples were then run on a Bioanalyzer todetermine cDNA concentrations. Gene expression libraries (GEX libraries) were prepared as recommended by the 10X Genomics Chromium Single Cell 3′ Reagent Kits User Guide (v3.1 Chemistry Dual Index) with appropriate modifications to the PCR cycles based on the calculated cDNA concentration. For sample preparation on the 10× Genomics platform, the Chromium Next GEM Single Cell 3′ Kit v3.1 (PN-1000268), Chromium Next GEM Chip G Single Cell Kit, (PN-1000120), and Dual Index Kit TT Set A, (PN-1000215) were used. The concentration of each library was determined through qPCR utilizing the KAPA library Quantification Kit according to the manufacturer's protocol (KAPA Biosystems/Roche) to produce cluster counts appropriate for the Illumina NovaSeq6000 instrument. Normalized libraries were sequenced on a NovaSeq6000 S4 Flow Cell using the XP workflow and a 50 × 10 × 16 × 150 sequencing recipe according to manufacturer protocol. A median sequencing depth of 50,000 reads/cell was targeted for each GEX library.

Preprocessing and quality control

The raw fastq files were processed with Cellranger-7.0.1 using the 10X mouse reference transcriptome, refdata-gex-mm10-2020-A, and the output matrix was input into Cellbender (Version 0.2.2) to remove ambient/background RNA. The cutoff we used for the number of expected cells was 10,000, and the number of total droplets was 15,000. The Cellbender filtered output count table was imported into R (version 4.1.0) and processed with the R package Seurat (version 4.3.0) (Stuart et al., 2019). As quality control, cells containing >10,000 molecules and <500 genes or >5% mitochondria detected were removed. The genes that were only detected in less than three cells were removed. The remaining data were further processed using Seurat. The integration was performed using the IntegrateData function from Seurat (Haghverdi et al., 2018; Stuart et al., 2019). The resulting corrected counts were used for all the downstream analyses.

Gene clustering and annotations

We performed principal component analysis (PCA) using 3,000 highly variable genes. The top 100 principal components were used to construct a shared nearest neighbor graph and modularity-based clustering using the Louvain algorithm was performed. The T-distributed stochastic neighbor embedding (TSNE) visualization was calculated based on the top 100 PCA, with perplexity of 30 as the number of targeted neighbors. Marker genes for every cell type were identified by comparing the expression of each gene in each cell against the rest of the cells using Wilcox test. The genes with the highest $\log_2$ fold change scores along with the canonical markers were used to annotate each of the clusters. We detected 36 clusters, which were grouped and annotated based on the expression of known cell markers, and maternal and fetal cell identities were confirmed based on the respective expression of *Xist* or *Ddx3y*, respectively (Fig. S4, A–D; and Fig. 7 A). In clusters within the maternal compartment, we identified myeloid immune cells (Mat-Imm, cluster 13) based on the expression of *Ptprc*, *Cd74*, and *Lyz2* (Han et al., 2018), decidual natural killers (cluster 23) expressing *Ptprc*, *Gzmc*, and *Eomes* (Han et al., 2018; Nelson et al., 2016), Dec-Str (clusters 0, 11, and 33) expressing *Pgr* and *Pbx1* (Marsh and Blelloch, 2020; Zhou et al., 2021), Mat-Endot (clusters 16 and 30) expressing *Pecam1*, *Cd34*, and *Cd36* (Han et al., 2018; He et al., 2021), epithelial cells (clusters 31 and 19) expressing *Esr*, *Prap1*, and *Guca2b* (He et al., 2021; Zhou et al., 2021), and lymphoid cells (cluster 25) identified by the markers *Prox1* and *Lyve1* (He et al., 2021). In the fetal compartment, trophoblast cells were identified based on *Krt7* and/or *Tpbpa* expression (Marsh and Blelloch, 2020) and included SpT (clusters 5 and 8; *Prl3b1*$^+$, *Prl8a6*$^+$, and *Pcdh12*$^-$) (Marsh and Blelloch, 2020; Zhou et al., 2021), GlyC (clusters 2 and 12; *Prl3b1*$^-$, *Pcdh12*$^+$, and *Prune2*$^+$) (Marsh and Blelloch, 2020; Simmons and Cross, 2005), S-TGC (clusters 4, 6, and 15; *Prl3b1*$^+$ and *Ctsq*$^+$) (Marsh and Blelloch, 2020; Simmons et al., 2007), and the two layers of SynT, namely SynTI (cluster 10; *Tfrc*$^+$ and *Glis1*$^+$) and SynTII (cluster 22; *Vegfa*$^+$ and *Gcgr*$^+$) (Marsh and Blelloch, 2020). Cluster 9 was assigned to JZP based on the expression of *Gjb3*, and cluster 27 was identified as labyrinth trophoblast progenitors due to expression of *Epcam*, *Prap1*, and *Guca2b*. We did not detect other subtypes of TGCs, including P-TGCs, spiral artery TGCs, or canal TGCs, in part due to overlapping cell markers (Simmons et al., 2007), low abundance, and/or oversize nuclei that can be filtered out during sample preparation (Marsh and Blelloch, 2020; Nelson et al., 2016). Cluster 1 may represent a population of unique TGCs, as it showed enriched expression of *Tpbpa*, *Prl2b1*, and *Prl3b1*, along with *Prl8a2* and *Cryab* (Nelson et al., 2016). Cluster 34 was rendered as undetermined trophoblast cells (Troph-Undet), as it expressed *Tpbpa* and markers of both GlyCs and SpT. Clusters 20, 17, and 21 were identified as fetal mesenchyme based on expression of *Col1a2*, *Postn*, and *Acta2* (Marsh and Blelloch, 2020; Zhou et al., 2021), and clusters 3, 24, and 32 corresponded to Fetal-Endot based on expression of *Pecam1*, *Cd34*, and *Cd36* (Han et al., 2018; Marsh and Blelloch, 2020; Zhou et al., 2021). We identified clusters 14 and 28 as primitive endoderm based on the expression of *Gkn2* and *Gata4* (Han et al., 2018), clusters 7 and 18 as Yolk sac (Afp^{+} and $Apoa1^{+}$) (Han et al., 2018; Zhou et al., 2021), and cluster 34 as fetal erythroid, based on the markers *Hbb-y* and *Hbb-x* (Marsh and Blelloch, 2020; Zhou et al., 2021). Finally, two clusters that expressed both *Xist* and *Ddx3y* (cluster 29, Mix-Undet, and cluster 35 expressing *Ptprc*, Mix-Imm) were excluded from the downstream analysis; these may represent doublets or maternal and fetal populations sharing similar cell markers.

Differential gene expression analysis

To identify the changes in expression across conditions, we performed differential expression test using Wilcoxon test from Seurat. The false discovery rate (FDR) was calculated by the Bonferroni correction method, and significant genes were set as those with FDR of <0.05 and $\log_2$ fold change scores >1. To identify antiviral responses in clusters of interest, we selected 32 ISGs and VSGs that were highly upregulated after ZIKV infection in at least one cell cluster, as shown in volcano plots (Fig. 7, C and D; and GEO accession GSE269612).

Pathway analysis

DESeq (Version 1.40.2) was used to select the differential expressed genes between two groups with the cutoff of P adjusted value <0.05 and $\log_2$ fold change >1. These genes were then used to align to the Hallmark mouse pathway database Msigdbr (Version 7.5.1) with package fgsea (Version 1.26.0) and pathways with P adjusted value <0.05 were chosen as the significantly enriched pathways.

Multiplex analysis of gene expression by qPCR

WT and $Mavs^{-/-}$ samples obtained at 6 dpi were subjected to analysis of expression of selected ISGs (*Cxcl10*, *Irf7*, *Ifit1*, *Rsad2*, *Oasl2*, *Isg15*, *Irf3*, and *Ifnar1*). Decidual and placental RNA was isolated from tissue homogenates as described in the "qRT-PCR analysis of viral burden" section. Multiplexing was performed using the TaqPath 1-Step Multiplex Master Mix (No ROX) (A28522; Thermo Fisher Scientific) with 2 µl of RNA in a 10 µl reaction. ROX dye (12223012; ThermoFisher Scientific) was added in a 1/50 ratio as a passive reference dye. Primers and probe sets were purchased from Integrated DNA Technologies in a Probe:Primer1:Primer2 ratio of 2.5:5.0:5.0 nmoles and combined as indicated (Table S3). Analysis was performed by the 2−ΔΔCt method using *Gapdh* as a housekeeping gene. Baseline expression of each target gene was set as the average ΔCt of mock samples for each genotype (*Avg* $[\mathrm{Ct\ target{-}Ct}\ Gapdh]_{\mathrm{mock}}$).

Statistical analysis

Statistical significance was assigned to P values <0.05 using Prism version 10 (GraphPad). Tests, number of animals, mean and median values, and statistical comparison groups are indicated in the figures and figure legends.

Online supplemental material

Fig. S1 contains supporting data showing placental damage and inflammation after intravenous delivery of ZIKV in WT animals. Fig. S2 shows no effects of fetal-specific deletions of *Tlr7*, *Tlr9*, *Myd88*, *Sting*, or *Ifnlr* on placental and fetal viral burden. Fig. S3 provides supporting data showing MAVS and IFNAR1 signaling pathways regulate ZIKV cell tropism. Fig. S4 contains supporting data for the snRNAseq analysis. Fig. S5 provides supporting data illustrating cell-type-specific induction of ISGs after ZIKV infection. Tables S1, S2, and S3 provide genotyping and TaqMan primers, and reagents used for immunohistochemistry and ISH.

Data availability

All data supporting the findings of this study are available within the paper and from the corresponding author upon request. This paper does not include original code. The snRNAseq data has been deposited in NCBI's Gene Expression Omnibus (Barrett et al., 2013; Edgar et al., 2002) and are accessible through GEO Series accession number GSE269612. Any additional information required to reanalyze the data reported in this paper is available from the corresponding author upon request.

Acknowledgments

We thank Crystal Idleburg and Samantha Coleman Cathcart at the Washington University Musculoskeletal Research Center Histology and Morphometry Core (NIH P30 AR074992) for providing tissue sectioning services, Dr. Krzysztof Hyrc at the Washington University Alafi Neuroimaging Laboratory (NIH Shared Instrumentation Grant S10 RR027552) for imaging and scanning services, and Dr. Wandy Beatty at the Washington University Molecular Microbiology Imaging Facility for help with laser scanning confocal microscopy. We also acknowledge the Rheumatic Diseases Research Resource-Based Center (NIH P30 AR073752) for speed congenic analysis, and the Genome Technology Access Center at the McDonnell Genome Institute at Washington University School of Medicine for help with genomic analysis (supported by National Cancer Institute P30 CA91842). Finally, we thank members of the Boon and Diamond laboratory at Washington University School of Medicine (St. Louis, MO, USA) for reagents and scientific direction.

The studies were supported by NIH grants R01 AI14582804 and R01 AI1459604 (to M.S. Diamond). We acknowledge grant support from the NIH (DK131107) and Bill & Melinda Gates Foundation (INV-033564) for contributions to the snRNAseq data generation and analysis.

Author contributions: Y. Alippe: Conceptualization, Data curation, Formal analysis, Investigation, Methodology, Validation, Visualization, Writing—original draft, Writing—review & editing, L. Wang: Data curation, Formal analysis, Methodology, Software, Visualization, R. Coskun: Investigation, Methodology, Software, S.P. Muraro: Investigation, F.R. Zhao: Investigation, Writing—review & editing, M. Elam-Noll: Investigation, Methodology, J.M. White: Conceptualization, Investigation, Methodology, D.M. Vota: Formal analysis, Writing—review & editing, V.C. Hauk: Formal analysis, Writing—review & editing, J.I.

Gordon: Methodology, Resources, Writing—review & editing, S.A. Handley: Data curation, Formal analysis, Investigation, Methodology, Project administration, Resources, Software, Supervision, Validation, Visualization, Writing—review & editing, M.S. Diamond: Conceptualization, Funding acquisition, Methodology, Project administration, Resources, Supervision, Writing—original draft, Writing—review & editing.

Disclosures: M.S. Diamond reported personal fees from Inbios, Ocugen, Akagera Medicines, Merck, and GlaxoSmithKline, grants from Emergent Biosolutions, and personal fees and grants from Vir Biotechnology, IntegerBio, and Moderna outside the submitted work. No other disclosures were reported.

Submitted: 19 April 2024
Revised: 12 June 2024
Accepted: 26 June 2024

References

Ander, S.E., M.S. Diamond, and C.B. Coyne. 2019. Immune responses at the maternal-fetal interface. *Sci. Immunol.* 4:eaat6114. https://doi.org/10.1126/sciimmunol.aat6114

Ank, N., M.B. Iversen, C. Bartholdy, P. Staeheli, R. Hartmann, U.B. Jensen, F. Dagnaes-Hansen, A.R. Thomsen, Z. Chen, H. Haugen, et al. 2008. An important role for type III interferon (IFN-lambda/IL-28) in TLR-induced antiviral activity. *J. Immunol.* 180:2474–2485. https://doi.org/10.4049/jimmunol.180.4.2474

Ashary, N., A. Bhide, P. Chakraborty, S. Colaco, A. Mishra, K. Chhabria, M.K. Jolly, and D. Modi. 2020. Single-cell RNA-seq identifies cell subsets in human placenta that highly expresses factors driving pathogenesis of SARS-CoV-2. *Front. Cell Dev. Biol.* 8:783. https://doi.org/10.3389/fcell.2020.00783

Ashley, C.L., A. Abendroth, B.P. McSharry, and B. Slobedman. 2019. Interferon-independent upregulation of interferon-stimulated genes during human cytomegalovirus infection is dependent on IRF3 expression. *Viruses*. 11:246. https://doi.org/10.3390/v11030246

Bankhead, P., M.B. Loughrey, J.A. Fernández, Y. Dombrowski, D.G. McArt, P.D. Dunne, S. McQuaid, R.T. Gray, L.J. Murray, H.G. Coleman, et al. 2017. QuPath: Open source software for digital pathology image analysis. *Sci. Rep.* 7:16878. https://doi.org/10.1038/s41598-017-17204-5

Barrett, T., S.E. Wilhite, P. Ledoux, C. Evangelista, I.F. Kim, M. Tomashevsky, K.A. Marshall, K.H. Phillippy, P.M. Sherman, M. Holko, et al. 2013. NCBI GEO: Archive for functional genomics data sets--update. *Nucleic Acids Res.* 41:D991–D995. https://doi.org/10.1093/nar/gks1193

Barrozo, E.R., M.D. Seferovic, E.C.C. Castro, A.M. Major, D.N. Moorshead, M.D. Jochum, R.F. Rojas, C.D. Shope, and K.M. Aagaard. 2023a. SARS-CoV-2 niches in human placenta revealed by spatial transcriptomics. *Med.* 4:612–634.e4. https://doi.org/10.1016/j.medj.2023.06.003

Barrozo, E.R., M.D. Seferovic, M.P. Hamilton, D.N. Moorshead, M.D. Jochum, T. Do, D.S. O'Neil, M.A. Suter, and K.M. Aagaard. 2023b. Zika virus co-opts microRNA networks to persist in placental niches detected by spatial transcriptomics. *Am. J. Obstet. Gynecol.* 230:251.e1–251.e17. https://doi.org/10.1016/j.ajog.2023.08.012

Bayer, A., E. Delorme-Axford, C. Sleigher, T.K. Frey, D.W. Trobaugh, W.B. Klimstra, L.A. Emert-Sedlak, T.E. Smithgall, P.R. Kinchington, S. Vadia, et al. 2015. Human trophoblasts confer resistance to viruses implicated in perinatal infection. *Am. J. Obstet. Gynecol.* 212:71.e71–71.e78. https://doi.org/10.1016/j.ajog.2014.07.060

Bhatnagar, J., D.B. Rabeneck, R.B. Martines, S. Reagan-Steiner, Y. Ermias, L.B. Estetter, T. Suzuki, J. Ritter, M.K. Keating, G. Hale, et al. 2017. Zika virus RNA replication and persistence in brain and placental tissue. *Emerg. Infect. Dis.* 23:405–414. https://doi.org/10.3201/eid2303.161499

Bohm, E.K., J.T. Vangorder-Braid, A.S. Jaeger, R.V. Moriarty, J.J. Baczenas, N.C. Bennett, S.L. O'Connor, M.K. Fritsch, N.A. Fuhler, K.K. Noguchi, and M.T. Aliota. 2021. Zika virus infection of pregnant Ifnar1$^{-/-}$ mice triggers strain-specific differences in fetal outcomes. *J. Virol.* 95:e0081821. https://doi.org/10.1128/JVI.00818-21

Brasil, P., J.P. Pereira Jr., M.E. Moreira, R.M. Ribeiro Nogueira, L. Damasceno, M. Wakimoto, R.S. Rabello, S.G. Valderramos, U.A. Halai, T.S. Salles, et al. 2016. Zika Virus Infection in Pregnant Women in Rio de Janeiro. *N. Engl. J. Med.* 375:2321–2334. https://doi.org/10.1056/NEJMoa1602412

Brien, J.D., H.M. Lazear, and M.S. Diamond. 2013. Propagation, quantification, detection, and storage of West Nile virus. *Curr. Protoc. Microbiol.* 31:15D 13 11–15D 13 18. https://doi.org/10.1002/9780471729259.mc15d03s31

Cao, B., M.S. Diamond, and I.U. Mysorekar. 2017. Maternal-fetal transmission of Zika virus: Routes and signals for infection. *J. Interferon Cytokine Res.* 37:287–294. https://doi.org/10.1089/jir.2017.0011

Carbaugh, D.L., S. Zhou, W. Sanders, N.J. Moorman, R. Swanstrom, and H.M. Lazear. 2020. Two genetic differences between closely related Zika virus strains determine pathogenic outcome in mice. *J. Virol.* 94:e00618-20. https://doi.org/10.1128/JVI.00618-20

Casazza, R.L., D.T. Philip, and H.M. Lazear. 2022. Interferon lambda signals in maternal tissues to exert protective and pathogenic effects in a gestational stage-dependent manner. *MBio*. 13:e0385721. https://doi.org/10.1128/mbio.03857-21

Chang, H.-W., E.M. Lee, Y. Wang, C. Zhou, K.M. Pruss, S. Henrissat, R.Y. Chen, C. Kao, M.C. Hibberd, H.M. Lynn, et al. 2024. Prevotella copri and microbiota members mediate the beneficial effects of a therapeutic food for malnutrition. *Nat. Microbiol.* 9:922–937. https://doi.org/10.1038/s41564-024-01628-7

Chen, Q., D. Shan, Y. Xie, X. Luo, Y. Wu, Q. Chen, R. Dong, and Y. Hu. 2023. Single cell RNA sequencing research in maternal fetal interface. *Front. Cell Dev. Biol.* 10:1079961. https://doi.org/10.3389/fcell.2022.1079961

Coyne, C.B., and H.M. Lazear. 2016. Zika virus: Reigniting the TORCH. *Nat. Rev. Microbiol.* 14:707–715. https://doi.org/10.1038/nrmicro.2016.125

Cugola, F.R., I.R. Fernandes, F.B. Russo, B.C. Freitas, J.L. Dias, K.P. Guimarães, C. Benazzato, N. Almeida, G.C. Pignatari, S. Romero, et al. 2016. The Brazilian Zika virus strain causes birth defects in experimental models. *Nature*. 534:267–271. https://doi.org/10.1038/nature18296

DeFilippis, V.R., B. Robinson, T.M. Keck, S.G. Hansen, J.A. Nelson, and K.J. Früh. 2006. Interferon regulatory factor 3 is necessary for induction of antiviral genes during human cytomegalovirus infection. *J. Virol.* 80:1032–1037. https://doi.org/10.1128/JVI.80.2.1032-1037.2006

Delorme-Axford, E., R.B. Donker, J.F. Mouillet, T. Chu, A. Bayer, Y. Ouyang, T. Wang, D.B. Stolz, S.N. Sarkar, A.E. Morelli, et al. 2013. Human placental trophoblasts confer viral resistance to recipient cells. *Proc. Natl. Acad. Sci. USA*. 110:12048–12053. https://doi.org/10.1073/pnas.1304718110

Detmar, J., I. Rovic, J. Ray, I. Caniggia, and A. Jurisicova. 2019. Placental cell death patterns exhibit differences throughout gestation in two strains of laboratory mice. *Cell Tissue Res.* 378:341–358. https://doi.org/10.1007/s00441-019-03055-1

Ding, Q., J.M. Gaska, F. Douam, L. Wei, D. Kim, M. Balev, B. Heller, and A. Ploss. 2018. Species-specific disruption of STING-dependent antiviral cellular defenses by the Zika virus NS2B3 protease. *Proc. Natl. Acad. Sci. USA*. 115:E6310–E6318. https://doi.org/10.1073/pnas.1803406115

Driggers, R.W., C.Y. Ho, E.M. Korhonen, S. Kuivanen, A.J. Jääskeläinen, T. Smura, A. Rosenberg, D.A. Hill, R.L. DeBiasi, G. Vezina, et al. 2016. Zika virus infection with prolonged maternal viremia and fetal brain abnormalities. *N. Engl. J. Med.* 374:2142–2151. https://doi.org/10.1056/NEJMoa1601824

Edgar, R., M. Domrachev, and A.E. Lash. 2002. Gene Expression Omnibus: NCBI gene expression and hybridization array data repository. *Nucleic Acids Res.* 30:207–210. https://doi.org/10.1093/nar/30.1.207

Elmore, S.A., R.Z. Cochran, B. Bolon, B. Lubeck, B. Mahler, D. Sabio, and J.M. Ward. 2022. Histology atlas of the developing mouse placenta. *Toxicol. Pathol.* 50:60–117. https://doi.org/10.1177/01926233211042270

Freyer, L., Y. Lallemand, P. Dardenne, A. Sommer, A. Biton, and E. Gomez Perdiguero. 2022. Erythro-myeloid progenitor origin of Hofbauer cells in the early mouse placenta. *Development*. 149:dev200104. https://doi.org/10.1242/dev.200104

Gorman, M.J., E.A. Caine, K. Zaitsev, M.C. Begley, J. Weger-Lucarelli, M.B. Uccellini, S. Tripathi, J. Morrison, B.L. Yount, K.H. Dinnon, 3rd, et al. 2018. An immunocompetent mouse model of Zika virus infection. *Cell Host Microbe*. 23:672–685 e676. https://doi.org/10.1016/j.chom.2018.04.003

Grant, A., S.S. Ponia, S. Tripathi, V. Balasubramaniam, L. Miorin, M. Sourisseau, M.C. Schwarz, M.P. Sánchez-Seco, M.J. Evans, S.M. Best, and A. García-Sastre. 2016. Zika virus targets human STAT2 to inhibit type I interferon signaling. *Cell Host Microbe*. 19:882–890. https://doi.org/10.1016/j.chom.2016.05.009

Guzeloglu-Kayisli, O., X. Guo, Z. Tang, N. Semerci, A. Ozmen, K. Larsen, D. Mutluay, S. Guller, F. Schatz, U.A. Kayisli, and C.J. Lockwood. 2020.

Zika virus-infected decidual cells elicit a gestational age-dependent innate immune response and exaggerate trophoblast Zika permissiveness: Implication for vertical transmission. *J. Immunol.* 205:3083–3094. https://doi.org/10.4049/jimmunol.2000713

Haghverdi, L., A.T.L. Lun, M.D. Morgan, and J.C. Marioni. 2018. Batch effects in single-cell RNA-sequencing data are corrected by matching mutual nearest neighbors. *Nat. Biotechnol.* 36:421–427. https://doi.org/10.1038/nbt.4091

Han, X., R. Wang, Y. Zhou, L. Fei, H. Sun, S. Lai, A. Saadatpour, Z. Zhou, H. Chen, F. Ye, et al. 2018. Mapping the mouse cell atlas by microwell-seq. *Cell.* 172:1091–1107.e17. https://doi.org/10.1016/j.cell.2018.02.001

He, J.-P., Q. Tian, Q.-Y. Zhu, and J.-L. Liu. 2021. Identification of intercellular crosstalk between decidual cells and niche cells in mice. *Int. J. Mol. Sci.* 22:7696. https://doi.org/10.3390/ijms22147696

Hemberger, M., C.W. Hanna, and W. Dean. 2020. Mechanisms of early placental development in mouse and humans. *Nat. Rev. Genet.* 21:27–43. https://doi.org/10.1038/s41576-019-0169-4

Isaac, S.M., M.B. Langford, D.G. Simmons, and S.L. Adamson. 2014. Anatomy of the mouse placenta throughout gestation. In The Guide to Investigation of Mouse Pregnancy. Academic Press, Cambridge, MA, USA. 69–73. https://doi.org/10.1016/B978-0-12-394445-0.00004-7

Jagger, B.W., J.J. Miner, B. Cao, N. Arora, A.M. Smith, A. Kovacs, I.U. Mysorekar, C.B. Coyne, and M.S. Diamond. 2017. Gestational stage and IFN-λ signaling regulate ZIKV infection in utero. *Cell Host Microbe.* 22:366–376.e3. https://doi.org/10.1016/j.chom.2017.08.012

Jiang, X., Y. Wang, Z. Xiao, L. Yan, S. Guo, Y. Wang, H. Wu, X. Zhao, X. Lu, and H. Wang. 2023. A differentiation roadmap of murine placentation at single-cell resolution. *Cell Discov.* 9:30. https://doi.org/10.1038/s41421-022-00513-z

Jurado, K.A., M.K. Simoni, Z. Tang, R. Uraki, J. Hwang, S. Householder, M. Wu, B.D. Lindenbach, V.M. Abrahams, S. Guller, and E. Fikrig. 2016. Zika virus productively infects primary human placenta-specific macrophages. *JCI Insight.* 1:e88461. https://doi.org/10.1172/jci.insight.88461

Karvas, R.M., S.A. Khan, S. Verma, Y. Yin, D. Kulkarni, C. Dong, K.-M. Park, B. Chew, E. Sane, L.A. Fischer, et al. 2022. Stem-cell-derived trophoblast organoids model human placental development and susceptibility to emerging pathogens. *Cell Stem Cell.* 29:810–825.e8. https://doi.org/10.1016/j.stem.2022.04.004

Kleber de Oliveira, W., J. Cortez-Escalante, W.T. De Oliveira, G.M. do Carmo, C.M. Henriques, G.E. Coelho, and G.V. Araújo de França. 2016. Increase in reported prevalence of microcephaly in infants born to women living in areas with confirmed Zika virus transmission during the first trimester of pregnancy: Brazil, 2015. *MMWR Morb. Mortal. Wkly. Rep.* 65:242–247. https://doi.org/10.15585/mmwr.mm6509e2

Kumar, A., S. Hou, A.M. Airo, D. Limonta, V. Mancinelli, W. Branton, C. Power, and T.C. Hobman. 2016. Zika virus inhibits type-I interferon production and downstream signaling. *EMBO Rep.* 17:1766–1775. https://doi.org/10.15252/embr.201642627

Kumar, H., T. Kawai, H. Kato, S. Sato, K. Takahashi, C. Coban, M. Yamamoto, S. Uematsu, K.J. Ishii, O. Takeuchi, and S. Akira. 2006. Essential role of IPS-1 in innate immune responses against RNA viruses. *J. Exp. Med.* 203:1795–1803. https://doi.org/10.1084/jem.20060792

Lazear, H.M., J. Govero, A.M. Smith, D.J. Platt, E. Fernandez, J.J. Miner, and M.S. Diamond. 2016. A mouse model of Zika virus pathogenesis. *Cell Host Microbe.* 19:720–730. https://doi.org/10.1016/j.chom.2016.03.010

Lazear, H.M., A. Lancaster, C. Wilkins, M.S. Suthar, A. Huang, S.C. Vick, L. Clepper, L. Thackray, M.M. Brassil, H.W. Virgin, et al. 2013. IRF-3, IRF-5, and IRF-7 coordinately regulate the type I IFN response in myeloid dendritic cells downstream of MAVS signaling. *PLoS Pathog.* 9:e1003118. https://doi.org/10.1371/journal.ppat.1003118

Lazear, H.M., J.W. Schoggins, and M.S. Diamond. 2019. Shared and distinct functions of type I and type III interferons. *Immunity.* 50:907–923. https://doi.org/10.1016/j.immuni.2019.03.025

Lee, A.J., and A.A. Ashkar. 2018. The dual nature of type I and type II interferons. *Front. Immunol.* 9:2061. https://doi.org/10.3389/fimmu.2018.02061

Lester, S.N., and K. Li. 2014. Toll-like receptors in antiviral innate immunity. *J. Mol. Biol.* 426:1246–1264. https://doi.org/10.1016/j.jmb.2013.11.024

Li, S., N. Qian, C. Jiang, W. Zu, A. Liang, M. Li, S.J. Elledge, and X. Tan. 2022. Gain-of-function genetic screening identifies the antiviral function of TMEM120A via STING activation. *Nat. Commun.* 13:105. https://doi.org/10.1038/s41467-021-27670-1

Liu, Y., B. Gordesky-Gold, M. Leney-Greene, N.L. Weinbren, M. Tudor, and S. Cherry. 2018. Inflammation-induced, STING-dependent autophagy restricts Zika virus infection in the Drosophila brain. *Cell Host Microbe.* 24:57–68.e3. https://doi.org/10.1016/j.chom.2018.05.022

Loo, Y.-M., and M. Gale Jr. 2011. Immune signaling by RIG-I-like receptors. *Immunity.* 34:680–692. https://doi.org/10.1016/j.immuni.2011.05.003

Ma, J., H. Ketkar, T. Geng, E. Lo, L. Wang, J. Xi, Q. Sun, Z. Zhu, Y. Cui, L. Yang, and P. Wang. 2018. Zika virus non-structural protein 4A blocks the RLR-MAVS signaling. *Front. Microbiol.* 9:1350. https://doi.org/10.3389/fmicb.2018.01350

Marsh, B., and R. Blelloch. 2020. Single nuclei RNA-seq of mouse placental labyrinth development. *Elife.* 9:e60266. https://doi.org/10.7554/eLife.60266

Miner, J.J., B. Cao, J. Govero, A.M. Smith, E. Fernandez, O.H. Cabrera, C. Garber, M. Noll, R.S. Klein, K.K. Noguchi, et al. 2016. Zika virus infection during pregnancy in mice causes placental damage and fetal demise. *Cell.* 165:1081–1091. https://doi.org/10.1016/j.cell.2016.05.008

Morrison, T.E., and M.S. Diamond. 2017. Animal models of Zika virus infection, pathogenesis, and immunity. *J. Virol.* 91:e00009-17. https://doi.org/10.1128/JVI.00009-17

Müller, U., U. Steinhoff, L.F. Reis, S. Hemmi, J. Pavlovic, R.M. Zinkernagel, and M. Aguet. 1994. Functional role of type I and type II interferons in antiviral defense. *Science.* 264:1918–1921. https://doi.org/10.1126/science.8009221

Nelson, A.C., A.W. Mould, E.K. Bikoff, and E.J. Robertson. 2016. Single-cell RNA-seq reveals cell type-specific transcriptional signatures at the maternal-foetal interface during pregnancy. *Nat. Commun.* 7:11414. https://doi.org/10.1038/ncomms11414

Pomar, L., V. Lambert, S. Matheus, C. Pomar, N. Hcini, G. Carles, D. Rousset, M. Vouga, A. Panchaud, and D. Baud. 2021. Prolonged maternal Zika viremia as a marker of adverse perinatal outcomes. *Emerg. Infect. Dis.* 27:490–498. https://doi.org/10.3201/eid2702.200684

Qu, D., A. McDonald, K.J. Whiteley, S.A. Bainbridge, and S.L. Adamson. 2014. Layer-enriched tissue dissection of the mouse placenta in late gestation. In The Guide to Investigation of Mouse Pregnancy. Academic Press, Cambridge, MA, USA. 529–535. https://doi.org/10.1016/B978-0-12-394445-0.00044-8

Quicke, K.M., J.R. Bowen, E.L. Johnson, C.E. McDonald, H. Ma, J.T. O'Neal, A. Rajakumar, J. Wrammert, B.H. Rimawi, B. Pulendran, et al. 2016. Zika virus infects human placental macrophages. *Cell Host Microbe.* 20:83–90. https://doi.org/10.1016/j.chom.2016.05.015

Rabelo, K., L.J. de Souza, N.G. Salomão, L.N. Machado, P.G. Pereira, E.A. Portari, R. Basílio-de-Oliveira, F.B. dos Santos, L.D. Neves, L.F. Morgade, et al. 2020. Zika induces human placental damage and inflammation. *Front. Immunol.* 11:2146. https://doi.org/10.3389/fimmu.2020.02146

Racicot, K., P. Aldo, A. El-Guindy, J.Y. Kwon, R. Romero, and G. Mor. 2017. Cutting edge: Fetal/placental type I IFN can affect maternal survival and fetal viral load during viral infection. *J. Immunol.* 198:3029–3032. https://doi.org/10.4049/jimmunol.1601824

Rivera-Serrano, E.E., A.S. Gizzi, J.J. Arnold, T.L. Grove, S.C. Almo, and C.E. Cameron. 2020. Viperin reveals its true function. *Annu. Rev. Virol.* 7:421–446. https://doi.org/10.1146/annurev-virology-011720-095930

Sarno, M., G.A. Sacramento, R. Khouri, M.S. do Rosário, F. Costa, G. Archanjo, L.A. Santos, N. Nery Jr., N. Vasilakis, A.I. Ko, and A.R.P. de Almeida. 2016. Zika virus infection and stillbirths: A case of hydrops fetalis, hydranencephaly and fetal demise. *PLoS Negl. Trop. Dis.* 10:e0004517. https://doi.org/10.1371/journal.pntd.0004517

Sheridan, M.A., D. Yunusov, V. Balaraman, A.P. Alexenko, S. Yabe, S. Verjovski-Almeida, D.J. Schust, A.W. Franz, Y. Sadovsky, T. Ezashi, and R.M. Roberts. 2017. Vulnerability of primitive human placental trophoblast to Zika virus. *Proc. Natl. Acad. Sci. USA.* 114:E1587–E1596. https://doi.org/10.1073/pnas.1616097114

Simmons, D.G., and J.C. Cross. 2005. Determinants of trophoblast lineage and cell subtype specification in the mouse placenta. *Dev. Biol.* 284:12–24. https://doi.org/10.1016/j.ydbio.2005.05.010

Simmons, D.G., A.L. Fortier, and J.C. Cross. 2007. Diverse subtypes and developmental origins of trophoblast giant cells in the mouse placenta. *Dev. Biol.* 304:567–578. https://doi.org/10.1016/j.ydbio.2007.01.009

Simmons, D.G., S. Rawn, A. Davies, M. Hughes, and J.C. Cross. 2008. Spatial and temporal expression of the 23 murine Prolactin/Placental Lactogen-related genes is not associated with their position in the locus. *BMC Genomics.* 9:352. https://doi.org/10.1186/1471-2164-9-352

Simoni, M.K., K.A. Jurado, V.M. Abrahams, E. Fikrig, and S. Guller. 2017. Zika virus infection of Hofbauer cells. *Am. J. Reprod. Immunol.* 77. https://doi.org/10.1111/aji.12613

Stirnweiss, A., A. Ksienzyk, K. Klages, U. Rand, M. Grashoff, H. Hauser, and A. Kröger. 2010. IFN regulatory factor-1 bypasses IFN-mediated antiviral effects through viperin gene induction. *J. Immunol.* 184:5179–5185. https://doi.org/10.4049/jimmunol.0902264

Stuart, T., A. Butler, P. Hoffman, C. Hafemeister, E. Papalexi, W.M. Mauck, 3rd, Y. Hao, M. Stoeckius, P. Smibert, and R. Satija. 2019. Comprehensive integration of single-cell data. *Cell.* 177:1888–1902.e1821. https://doi.org/10.1016/j.cell.2019.05.031

Suthar, M.S., S. Aguirre, and A. Fernandez-Sesma. 2013. Innate immune sensing of flaviviruses. *PLoS Pathog.* 9:e1003541. https://doi.org/10.1371/journal.ppat.1003541

Suy, A., E. Sulleiro, C. Rodó, É. Vázquez, C. Bocanegra, I. Molina, J. Esperalba, M.P. Sánchez-Seco, H. Boix, T. Pumarola, and E. Carreras. 2016. Prolonged Zika virus viremia during pregnancy. *N. Engl. J. Med.* 375:2611–2613. https://doi.org/10.1056/NEJMc1607580

Szaba, F.M., M. Tighe, L.W. Kummer, K.G. Lanzer, J.M. Ward, P. Lanthier, I.J. Kim, A. Kuki, M.A. Blackman, S.J. Thomas, and J.S. Lin. 2018. Zika virus infection in immunocompetent pregnant mice causes fetal damage and placental pathology in the absence of fetal infection. *PLoS Pathog.* 14:e1006994. https://doi.org/10.1371/journal.ppat.1006994

Tabata, T., M. Petitt, H. Puerta-Guardo, D. Michlmayr, E. Harris, and L. Pereira. 2018. Zika virus replicates in proliferating cells in explants from first-trimester human placentas, potential sites for dissemination of infection. *J. Infect. Dis.* 217:1202–1213. https://doi.org/10.1093/infdis/jix552

Tabata, T., M. Petitt, H. Puerta-Guardo, D. Michlmayr, C. Wang, J. Fang-Hoover, E. Harris, and L. Pereira. 2016. Zika virus targets different primary human placental cells, suggesting two routes for vertical transmission. *Cell Host Microbe.* 20:155–166. https://doi.org/10.1016/j.chom.2016.07.002

Ventura, C.V., M. Maia, V. Bravo-Filho, A.L. Góis, and R. Belfort Jr. 2016. Zika virus in Brazil and macular atrophy in a child with microcephaly. *Lancet.* 387:228. https://doi.org/10.1016/S0140-6736(16)00006-4

Vermillion, M.S., J. Lei, Y. Shabi, V.K. Baxter, N.P. Crilly, M. McLane, D.E. Griffin, A. Pekosz, S.L. Klein, and I. Burd. 2017. Intrauterine Zika virus infection of pregnant immunocompetent mice models transplacental transmission and adverse perinatal outcomes. *Nat. Commun.* 8:14575. https://doi.org/10.1038/ncomms14575

Villazana-Kretzer, D.L., K.M. Wuertz, D. Newhouse, J.R. Damicis, E.M. Dornisch, K.M. Voss, A.E. Muruato, J.A. Paymaster, S.S. Schmiedecke, S.M. Edwards, et al. 2022. ZIKV can infect human term placentas in the absence of maternal factors. *Commun. Biol.* 5:243. https://doi.org/10.1038/s42003-022-03158-6

Waggoner, J.J., L. Gresh, M.J. Vargas, G. Ballesteros, Y. Tellez, K.J. Soda, M.K. Sahoo, A. Nuñez, A. Balmaseda, E. Harris, and B.A. Pinsky. 2016. Viremia and clinical presentation in Nicaraguan patients infected with Zika virus, chikungunya virus, and dengue virus. *Clin. Infect. Dis.* 63:1584–1590. https://doi.org/10.1093/cid/ciw589

Wu, H., X.-Y. Huang, M.-X. Sun, Y. Wang, H.-Y. Zhou, Y. Tian, B. He, K. Li, D.-Y. Li, A.-P. Wu, et al. 2023. Zika virus targets human trophoblast stem cells and prevents syncytialization in placental trophoblast organoids. *Nat. Commun.* 14:5541. https://doi.org/10.1038/s41467-023-41158-0

Yang, L., E.C. Semmes, C. Ovies, C. Megli, S. Permar, J.B. Gilner, and C.B. Coyne. 2022. Innate immune signaling in trophoblast and decidua organoids defines differential antiviral defenses at the maternal-fetal interface. *Elife.* 11:e79794. https://doi.org/10.7554/eLife.79794

Yockey, L.J., K.A. Jurado, N. Arora, A. Millet, T. Rakib, K.M. Milano, A.K. Hastings, E. Fikrig, Y. Kong, T.L. Horvath, et al. 2018. Type I interferons instigate fetal demise after Zika virus infection. *Sci. Immunol.* 3:eaao1680. https://doi.org/10.1126/sciimmunol.aao1680

Yockey, L.J., L. Varela, T. Rakib, W. Khoury-Hanold, S.L. Fink, B. Stutz, K. Szigeti-Buck, A. Van den Pol, B.D. Lindenbach, T.L. Horvath, and A. Iwasaki. 2016. Vaginal exposure to Zika virus during pregnancy leads to fetal brain infection. *Cell.* 166:1247–1256.e1244. https://doi.org/10.1016/j.cell.2016.08.004

Zhao, H., E. Fernandez, K.A. Dowd, S.D. Speer, D.J. Platt, M.J. Gorman, J. Govero, C.A. Nelson, T.C. Pierson, M.S. Diamond, and D.H. Fremont. 2016. Structural basis of Zika virus-specific antibody protection. *Cell.* 166:1016–1027. https://doi.org/10.1016/j.cell.2016.07.020

Zhao, Z., Q. Li, U. Ashraf, M. Yang, W. Zhu, J. Gu, Z. Chen, C. Gu, Y. Si, S. Cao, and J. Ye. 2022. Zika virus causes placental pyroptosis and associated adverse fetal outcomes by activating GSDME. *Elife.* 11:e73792. https://doi.org/10.7554/eLife.73792

Zhou, X., Y. Xu, S. Ren, D. Liu, N. Yang, Q. Han, S. Kong, H. Wang, W. Deng, H. Qi, and J. Lu. 2021. Single-cell RNA-seq revealed diverse cell types in the mouse placenta at mid-gestation. *Exp. Cell Res.* 405:112715. https://doi.org/10.1016/j.yexcr.2021.112715

Zimmerman, M.G., K.M. Quicke, J.T. O'Neal, N. Arora, D. Machiah, L. Priyamvada, R.C. Kauffman, E. Register, O. Adekunle, D. Swieboda, et al. 2018. Cross-reactive dengue virus antibodies augment Zika virus infection of human placental macrophages. *Cell Host Microbe.* 24:731–742.e6. https://doi.org/10.1016/j.chom.2018.10.008

Supplemental material

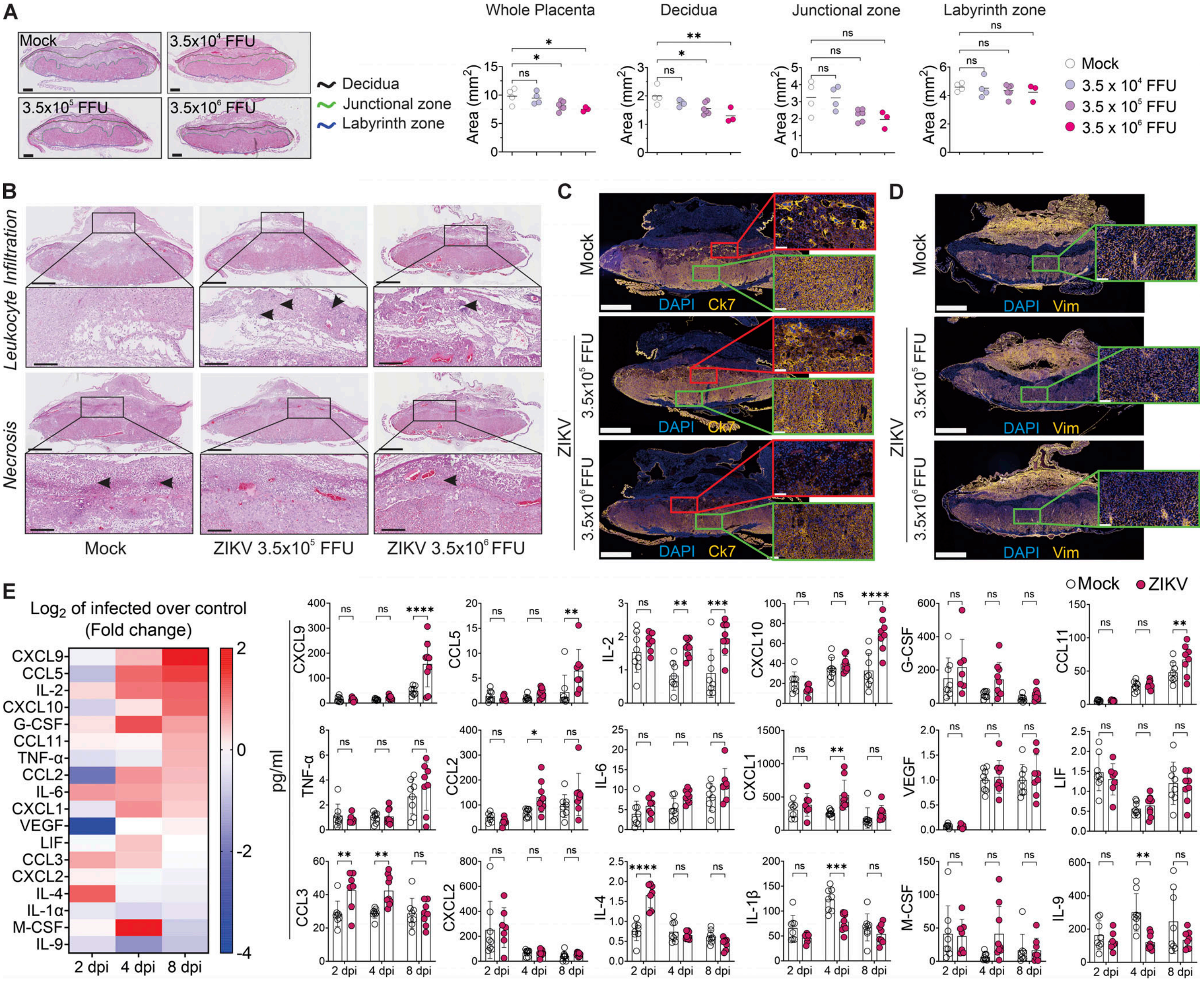

Figure S1. **ZIKV infection induces placental damage and inflammation, related to Figs. 1 and 2. (A)** Representative images of manually defined placental areas (scale bars: 500 µm) and quantification of placental, decidual, junctional zone, and labyrinth zone areas, excluding the maternal triangle and the chorionic plate. Each data point represents the average of at least two tissue sections from the same placenta; $n = 4$ (mock and 3.5×10^4 FFU), $n = 6$ (3.5×10^5 FFU), and $n = 3$ (3.5×10^6 FFU) placentas from two dams per group. **(B)** Representative images of deciduitis (black arrows, top panel) and necrosis (black arrows, bottom panel) in mock- and ZIKV-infected (3.5×10^5 and 3.5×10^6 FFU) placentas, at 8 dpi. Placenta images at 2.5× magnification (scale bars: 1 mm); insets at 10× magnification (scale bars: 250 µm). Insets denoting leukocyte infiltration and necrosis in placentas infected with 3.5×10^6 FFU ZIKV show different areas from the same sample. Data from two experiments, $n = 4$ (mock), $n = 6$ (3.5×10^5 FFU), and $n = 3$ (3.5×10^6 FFU) placentas from two dams per group. **(C)** Representative images of immunostaining for the pan-trophoblast marker CK7 in mock- and ZIKV-infected WT placentas at 8 dpi counterstained with DAPI. Placenta images taken at 2.5× magnification (scale bars: 1 mm), and insets to show the junctional zone (red rectangles) and labyrinth zone (green rectangles) at 20× (scale bars: 100 µm). **(D)** Representative images of immunostaining for vimentin (endothelial and mesenchymal cells) in mock- and ZIKV-infected WT placentas at 8 dpi and counterstained with DAPI. Placenta images at 2.5× magnification (scale bars: 1 mm), and selected areas showing the labyrinth zone (green rectangles) at 20× magnification (scale bars: 100 µm). **(C and D)** $n = 3$–5 placentas from two dams per group (two experiments). **(E)** Cytokine levels in the fetal compartment of WT placentas at 2 dpi (E11.5), 4 dpi (E13.5), and 8 dpi (E17.5) after inoculation with 3.5×10^6 FFU of ZIKV. For each cytokine, the $\log_2$ fold change was calculated compared with mock-infected animals. Samples were pooled from two experiments with $n = 8$ placentas from two dams per group. Statistical analysis: (A) One-way ANOVA with Dunnett's post-test (comparison to mock; (*$P < 0.05$, **$P < 0.01$, ns, not significant); (E) two-way ANOVA with Sidak's multiple comparison test (comparison to mock for each time point; *$P < 0.05$, **$P < 0.01$, ***$P < 0.001$, ****$P < 0.0001$, ns, not significant).

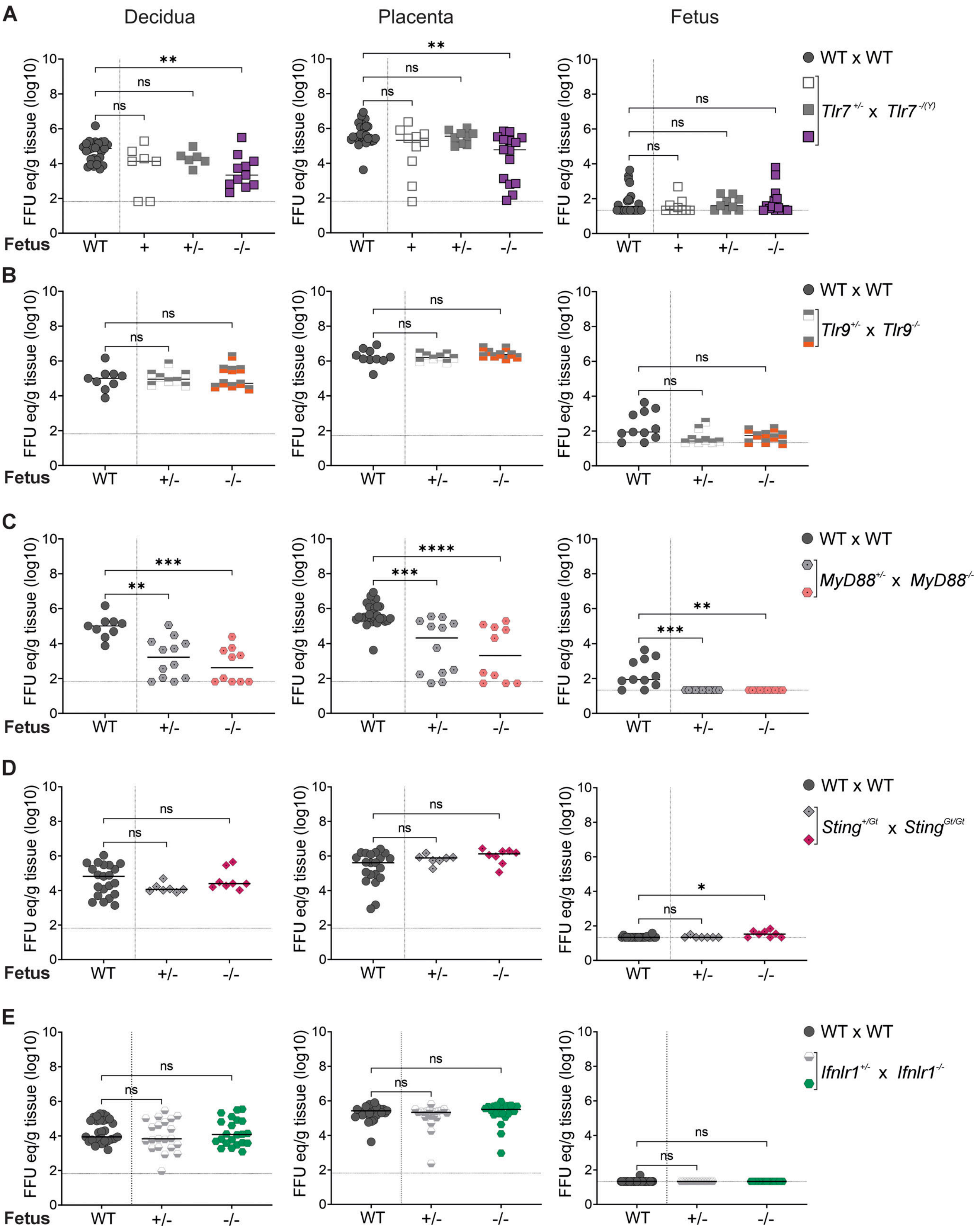

Figure S2. **Effects of placental innate immune pathways on ZIKV infection and vertical transmission, related to Fig. 3. (A–E)** Mice were mated as indicated and inoculated via intravenous injection at E9.5 with 3.5×10^5 FFU of ZIKV. ZIKV RNA levels were measured at 8 dpi. (A) *Tlr7*$^{+/-}$ × *Tlr7*$^{-/(Y)}$, (B) *Tlr9*$^{+/-}$ × *Tlr9*$^{-/-}$, (C) *Myd88*$^{+/-}$ × *Myd88*$^{-/-}$, (D) *Sting*$^{+/-}$ × *Sting*$^{-/-}$, and (E) *Ifnlr1*$^{+/-}$ × *Ifnlr1*$^{-/-}$ crosses. Data are pooled from two experiments (*n* = 4 dams (WT × WT) and *n* = 2 dams per group). Dotted horizontal lines represent the LOD. Statistical analysis: Kruskal–Wallis test with Dunn's post-test (comparison to samples from WT × WT matings; $^{*}P < 0.05$, $^{**}P < 0.01$, $^{***}P < 0.001$, $^{****}P < 0.0001$, ns, not significant).

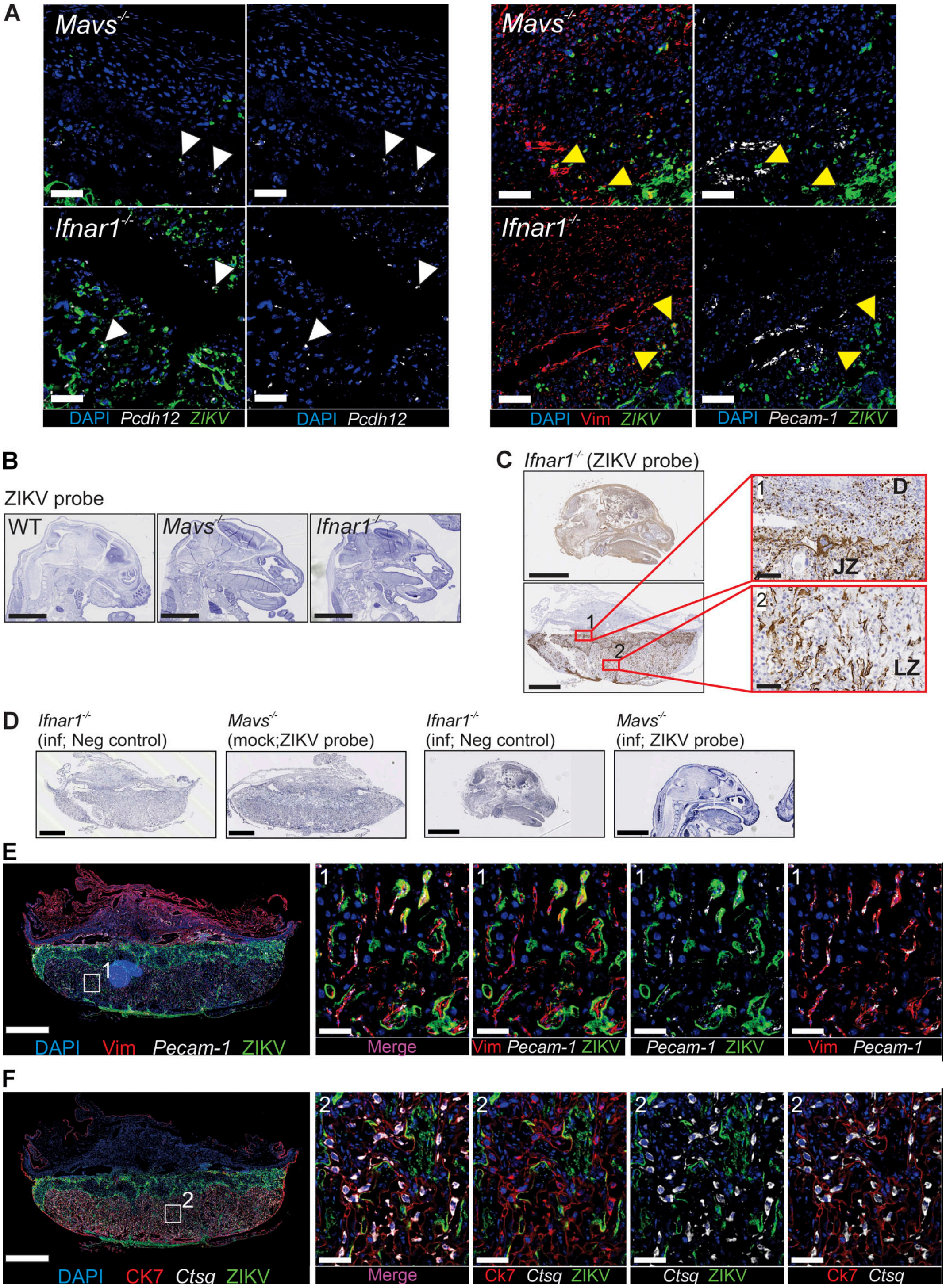

Figure S3. **ZIKV infection at the maternal–fetal interface in placentas with gene defects in innate immune signaling, related to Fig. 5. (A)** FISH for *Pcdh12* and ZIKV (left panel) or for *CD31* (*Pecam-1*) and ZIKV combined with immunofluorescence for vimentin (right panel). Maximum projection of three to four confocal Z-stacks taken at 20× magnification of the decidua, and insets zoomed 200% (scale bars: 50 µm); white arrowheads, GlyC; yellow arrowheads, Dec-Str cells. Data are representative of two placentas for each condition from two dams. **(B–D)** ISH of ZIKV RNA in ZIKV-infected WT, *Mavs*$^{-/-}$, or *Ifnar1*$^{-/-}$ fetuses showing undetectable ZIKV RNA in most of the analyzed samples (B), and an infrequent case of staining of the labyrinth zone (LZ) and fetus (C). Placenta and fetal head images at 2.5× magnification (scale bars: 1 and 2.5 mm, respectively); insets at 20× magnification (scale bars: 100 µm). Corresponding negative controls (negative probe and ZIKV probes in mock samples) are shown (D). D, decidua; JZ, junctional zone. **(E and F)** Combined FISH and immunofluorescence staining of the samples shown in C with FISH for *CD31* (*Pecam-1*) and ZIKV RNA combined with vimentin immunostaining (E), and for *Ctsq* and ZIKV RNA combined with CK7 immunostaining (F). Placenta images at 2.5× magnification (scale bars: 1 mm); insets are the maximum projection of three to four confocal Z-stacks taken at 20× magnification (scale bars: 50 µm); numbers indicate the corresponding inset. **(B–F)** Images are representative of $n = 2$ experiments (two dams per group; $n = 4$ WT, 5 *Mavs*$^{-/-}$, and 6 *Ifnar1*$^{-/-}$ fetuses, from which one *Mavs*$^{-/-}$ and two *Ifnar1*$^{-/-}$ fetuses were nonviable at the time of collection.

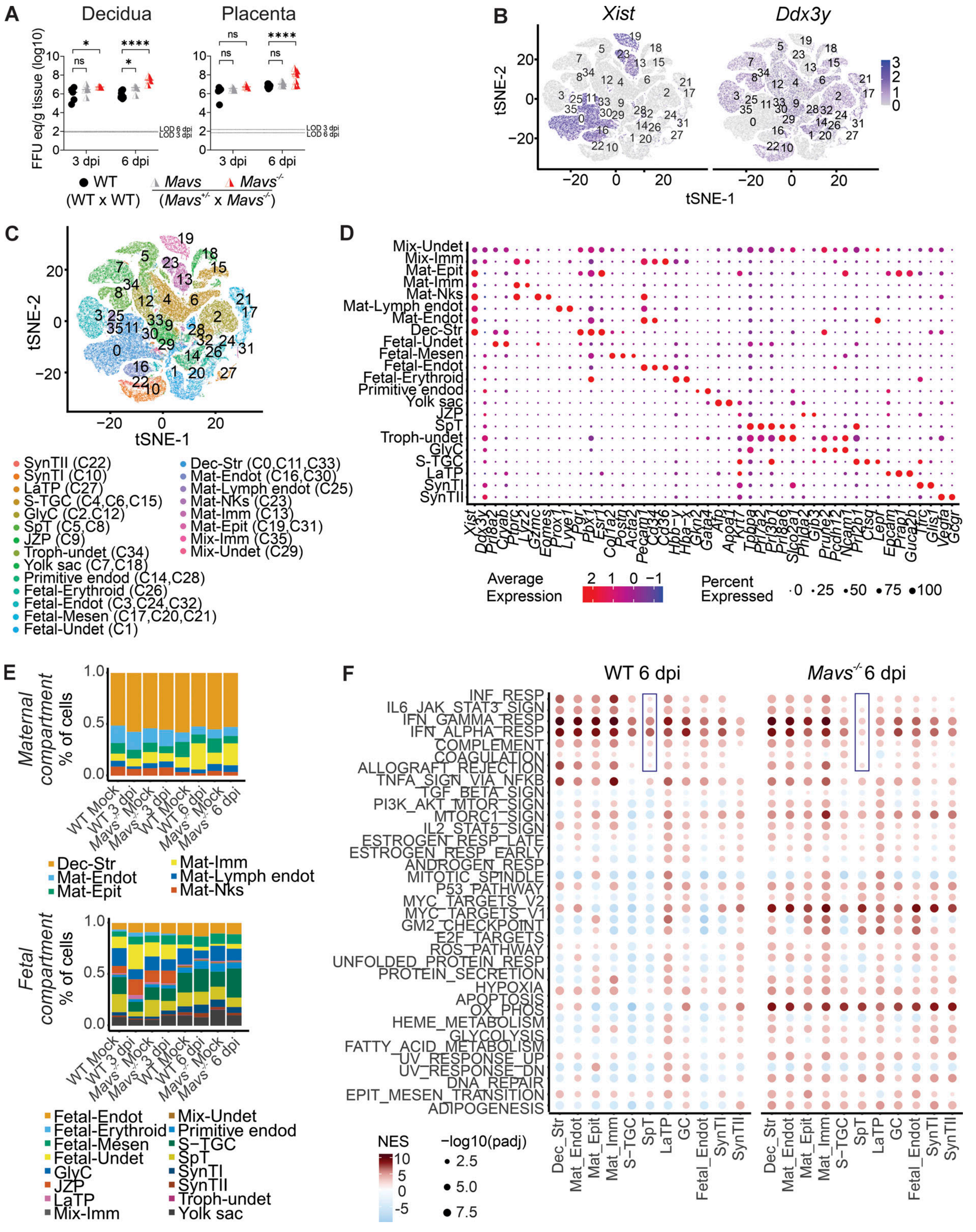

Figure S4. **snRNAseq of WT and *Mavs*$^{-/-}$ placentas, related to** Figs. 7, 8, 9, and 10**.** **(A)** Viral loads at E9.5 in placenta and decidua at 3 or 6 dpi. Data are from two experiments, including littermates of those used for snRNAseq, and samples are pooled from two dams per group. **(B and C)** TSNE plots of the 98,661 nuclei captured by micro-droplet assay (10X Genomics), showing the differential expression of *Xist* and *Ddx3y* in maternal and fetal clusters, respectively (B), and plot grouped based on shared prototypical cell markers (C). **(D)** Bubble plot showing the average expression (color scale) and percentage of nuclei (node size) in each cluster expressing canonical markers used for identification of cell types. **(E)** Bar plot of the relative proportion of each cell type in mock- and ZIKV-infected WT or *Mavs*$^{-/-}$ placentas, collected at E12.5 and E15.5 (3 and 6 dpi, respectively) in the maternal (top panel) and fetal (bottom panel) compartments. **(F)** Bubble plots showing ZIKV-induced modulation of Hallmark pathways (gene set enrichment analysis) in WT and *Mavs*$^{-/-}$ placentas at 6 dpi. LaTP, labyrinth precursors. Statistical analysis (A): Two-way ANOVA and Dunnett's post-test (comparison to samples from WT × WT matings at each time point; *P < 0.05, ****P < 0.0001, ns, not significant).

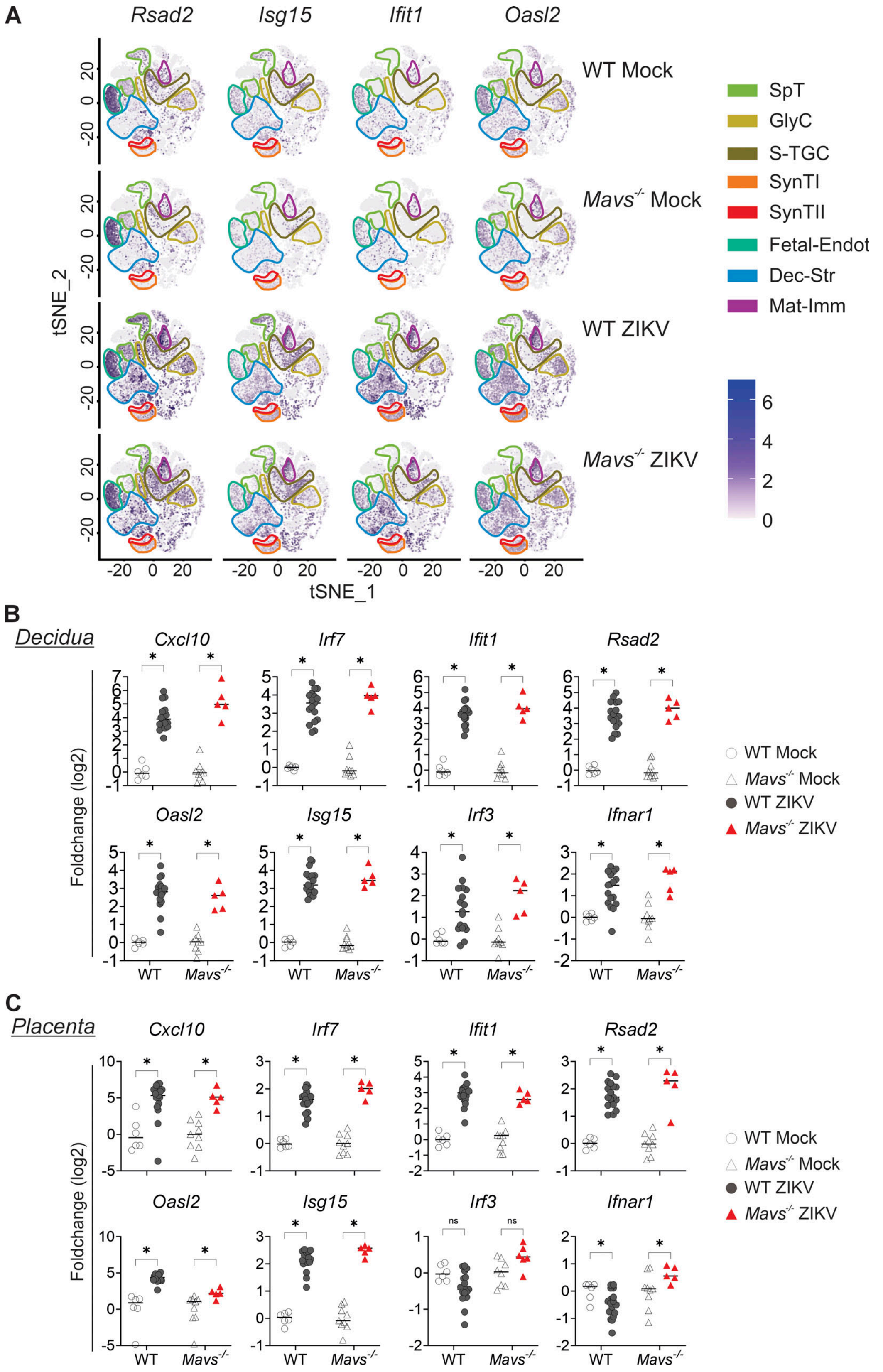

Figure S5. **ZIKV infection modulates expression of ISGs in a cell-specific manner, related to Figs. 7, 8, 9, and 10. (A)** Feature plots of *Rsad2*, *Isg15*, *Ifit1*, and *Oasl2* RNA expression in mock- and ZIKV-infected WT or *Mavs*$^{-/-}$ placentas at 6 dpi (E15.5). Selected clusters are highlighted with colored outlines. **(B and C)** Multiplex analysis by qPCR of selected ISGs at 6 dpi in deciduas (B) and fetal placentas (C) from WT and *Mavs*$^{-/-}$ fetuses compared with their corresponding mock controls. Data are from two independent experiments, two to three dams per group and condition. Statistical analysis (B and C): Multiple Mann–Whitney test with Holm–Sidak correction ($*P_{adj} < 0.001$).

Provided online are three tables. Table S1 lists primers for in-house PCR genotyping. Table S2 shows reagents for immunofluorescence and ISH. Table S3 lists primer/probe combinations for multiplex qPCR.